

STUDY OF SHOCK WAVE BOUNDARY LAYER INTERACTION PHENONEMON USING
COLOR SCHLIEREN AND SNAPSHOT PROPER ORTHOGONAL DECOMPOSITION

by

NARENDRA CHAGANTI SUBRAHMANYA DATTA

DR. SEMIH OLCMEN, COMMITTEE CHAIR
DR. MUHAMMAD ALI ROB SHARIF
DR. KEITH WILLIAMS

A THESIS

Submitted in partial fulfillment of the requirements
for the degree of Master of Science
in the Department of Aerospace Engineering and Mechanics
in the Graduate School of
The University of Alabama

TUSCALOOSA, ALABAMA

2013

Copyright Narendra Chaganti Subrahmanya Datta 2013
ALL RIGHTS RESERVED

ABSTRACT

The flow structure of shockwave boundary layer interaction (SWBLI) has been studied using Rainbow Schlieren Deflectometry (RSD), Ensemble Averaging, Fast Fourier Transform (FFT), and snapshot Proper Orthogonal Decomposition (POD) techniques. The Mach number of the approach free-stream was $Mach = 3$. Shockwave was generated with a 12° wedge. The color schlieren pictures are used to determine the transverse ray deflections at each pixel of the pictures taken using a high speed camera. The interaction region structure is described statistically with the ensemble average and, root mean square deflections. FFT technique is used to determine the dominant frequencies at different regions of the flow field. Results indicate that low frequency oscillations dominate the flow field. The POD technique results complement the findings of the ensemble averaging technique and show that distinct regions contain most of the energy in the flow field. These distinct regions are located around the reflected shock, around the shock wave reaching into the approach boundary layer and around the separation region over the edge of the separation bubble.

DEDICATION

To my dear parents

Sri C. Radhakrishna and Smt. N.L.S.P. Vardhani

and my brother

Sri Sudheendra V.K. Chaganti

LIST OF ABBREVIATIONS AND SYMBOLS

| | |
|----------------------|--|
| d | Transverse ray displacement |
| f_c | Focal length of decollimating lens |
| ε | Deflection angle |
| M | Mach number |
| ρ | Density |
| L | Width of the test medium |
| k | Gladstone-Dale constant |
| P | Pressure |
| R | Gas constant |
| T | Temperature |
| n | Refractive index of air |
| $\overline{d_{i,j}}$ | Ensemble average deflection at pixel location given by i,j indices |
| $\sigma_{i,j}$ | Standard deviation of the displacement |
| n_1 | number of grid points in the x coordinate axis |
| n_2 | number of grid points in the y coordinate axis |
| H | Deflection matrix |
| X_{lm} | Coordinate variables |
| $t_{i/j}$ | Time |
| $[R]_{ij}$ | Time correlation tensor |

| | |
|-------------------|--|
| A^n | Eigen vector matrix |
| a^n | POD coefficients |
| λ^n | n^{th} Eigen value |
| E | Energy associated with flow field |
| N | Number of Eigen modes |
| $\Phi^{(n)}$ | POD mode |
| $H(X, t_k)$ | Member of the flow field |
| $\hat{H}(X, t_k)$ | Highest energy mode |
| S | Strouhal number |
| f | Dominant frequency considered near the foot of the reflected shock, recirculation and close to wall regions |
| L | Length of the interaction which is average distance between foot of reflected shock and extrapolated incident shock wave position on the wall. |
| U | Free stream velocity |

ACKNOWLEDGMENTS

I am pleased to have this opportunity to thank the many colleagues, friends, and faculty members who have helped me with this research project. I am most indebted to Dr. Semih Olcmen, the chairman of this thesis, for sharing his research expertise and wisdom regarding the motivational theory. I would like to take this opportunity to thank Dr. Semih Olcmen for guiding me in this research especially in the experimentation phase. I would also like to thank all of my committee members, Dr. Muhammad Ali Rob Sharif, Dr. Keith Williams for their invaluable input and support of both the thesis and my academic progress. I would like to thank Tim Connell for all the help he rendered during various stages of experimental setup. I would also extend my gratitude to group members for their assistance in collecting data.

I would also like to thank Dr. Pankaj Kolhe for sharing his knowledge in the area of color schlieren technique.

This research would not have been possible without the support of my friends and fellow graduate students and of course of my family who never stopped encouraging me to persist. Finally I thank all of them who have directly or indirectly helped me during my study and stay at The University of Alabama.

CONTENTS

| | |
|---|-----|
| ABSTRACT | ii |
| DEDICATION | iii |
| LIST OF ABBREVIATIONS AND SYMBOLS..... | iv |
| ACKNOWLEDGMENTS | vi |
| LIST OF TABLES | ix |
| LIST OF FIGURES | x |
| 1. INTRODUCTION | 1 |
| 1.1 About SWBLI..... | 1 |
| 1.2 Types of shock boundary layer interactions | 2 |
| 1.3 Control techniques | 6 |
| 2. LITERATURE REVIEW | 8 |
| 3. EXPERIMENTAL SETUP..... | 15 |
| 3.1 Wind tunnel | 15 |
| 3.1.1 Storage tank and compressors..... | 15 |
| 3.1.2 Pressure regulator and stagnation chamber | 16 |
| 3.1.3 Nozzle and test section | 17 |
| 3.1.4 Diffuser..... | 19 |
| 3.2 Color schlieren apparatus | 19 |
| 4. ANALYSIS PROCEDURE | 23 |
| 4.1 Color schlieren analysis | 23 |
| 4.2 Fourier transform | 29 |

| | |
|--|----|
| 4.3 Snapshot proper orthogonal decomposition | 30 |
| 5. RESULTS AND DISCUSSION..... | 32 |
| 5.1 Color schlieren results..... | 32 |
| 5.2 Fourier transform results | 38 |
| 5.3 Snapshot proper orthogonal decomposition results | 55 |
| 6. CONCLUSION AND FUTURE WORK | 66 |
| REFERENCES..... | 68 |
| APPENDIX A: EXPERIMENTAL CONDITIONS | 71 |
| APPENDIX B: ENERGY ASSOCIATED WITH POD MODES..... | 72 |
| APPENDIX C: MATLAB CODE FOR DATA REDUCTION | 73 |

LIST OF TABLES

| | |
|---|----|
| A.1 Input pressure and temperature..... | 71 |
| A.2 Pressure regulator values..... | 71 |
| B.1 Energy associated with the POD modes..... | 72 |

LIST OF FIGURES

| | |
|---|----|
| 1.1 2D Compression Corner..... | 2 |
| 1.2 Shock impingement | 3 |
| 1.3 2D Expansion-Compression corner | 4 |
| 1.5 3D Single Fin..... | 4 |
| 1.6 3D Double Fin | 5 |
| 3.1 Schematic drawing of the wind tunnel..... | 15 |
| 3.2 Dryers..... | 16 |
| 3.3 Compressors | 16 |
| 3.4 Solidworks cut section view of the wind tunnel..... | 18 |
| 3.5 Solidworks cut section view of the test section..... | 18 |
| 3.6 Actual setting of the wind tunnel assembly | 19 |
| 3.7 Schematic of color schlieren apparatus..... | 20 |
| 3.8 Actual setting of the color schlieren apparatus | 20 |
| 3.9 Color filter | 20 |
| 4.1 Filter calibration curve | 24 |
| 4.2 Refined calibration curve | 25 |
| 4.3 Background image | 26 |
| 4.4 Test image | 27 |
| 4.5 Cropped test image | 27 |
| 5.1 Ensemble average deflection lengths..... | 32 |
| 5.2 Detailed flow structure of shock boundary layer interaction | 33 |

| | |
|--|----|
| 5.3 Average density gradients | 35 |
| 5.4 Average density | 36 |
| 5.5 RMS fluctuating deflection length..... | 37 |
| 5.6 RMS fluctuating density gradient..... | 37 |
| 5.7 Pixel wise maximum frequencies | 39 |
| 5.8 Pixel wise peak frequency distribution | 39 |
| 5.9 Power spectrum at 9.76Hz | 40 |
| 5.10 Power spectrum at 14.65Hz..... | 40 |
| 5.11 Power spectrum at 24.41Hz..... | 41 |
| 5.12 Power spectrum at 48.82Hz..... | 42 |
| 5.13 Power spectrum at 73.24Hz..... | 42 |
| 5.14 Power spectrum at 97.66Hz..... | 43 |
| 5.15 Power spectrum at 122.07Hz..... | 44 |
| 5.16 Power spectrum at 146.49Hz..... | 44 |
| 5.17 Power spectrum at 170.90Hz..... | 45 |
| 5.18 Power spectrum at 195.32Hz..... | 46 |
| 5.19 Power spectrum at 219.73Hz..... | 46 |
| 5.20 Power spectrum at 244.15Hz..... | 47 |
| 5.21 Power spectrum at 268.56Hz..... | 47 |
| 5.22 Power spectrum at 292.98Hz..... | 48 |
| 5.23 Power spectrum at 317.39Hz..... | 49 |
| 5.24 Power spectrum at 341.81Hz..... | 49 |
| 5.25 Power spectrum at 390.64Hz..... | 50 |

| | |
|---|----|
| 5.26 Power spectrum at 415.05Hz..... | 50 |
| 5.27 Power spectrum at 439.47Hz..... | 51 |
| 5.28 Power spectrum at 463.88Hz..... | 51 |
| 5.29 Power spectrum at 488.30Hz..... | 52 |
| 5.30 Power spectrum at 500Hz | 52 |
| 5.31 Edge detection of the color schlieren images | 54 |
| 5.32 Average deflection length calculated using most energetic mode | 57 |
| 5.33 Average deflection length calculated using the other modes | 58 |
| 5.34 Average deflection length calculated using the second highest energy mode | 59 |
| 5.35 Average deflection length calculated using the third highest energy mode | 59 |
| 5.36 Average deflection length calculated using the fourth highest energy mode | 60 |
| 5.37 Average deflection length calculated using the fifth highest energy mode | 61 |
| 5.38 Average deflection length calculated using the sixth highest energy mode | 61 |
| 5.39 Average deflection length calculated using the seventh highest energy mode | 62 |
| 5.40 Average deflection length calculated using the eighth highest energy mode | 63 |
| 5.41 Average deflection length calculated using the ninth highest energy mode | 63 |
| 5.42 Average deflection length calculated using the tenth highest energy mode | 64 |

CHAPTER 1

INTRODUCTION

This chapter covers about the overview of the research topic, possible types of shock wave boundary layer interactions and brief overview of control techniques.

1.1 About SWBLI

There are many challenges that are faced in the high speed flight. One such challenge is due to shockwaves. Shockwaves which are produced at the supersonic speeds cause discontinuity in the flow field and affects the characteristics of air, such as the pressure across a shock increases and velocity decreases and hence causes drag. The study of the shock wave interaction with the boundary layer near the surfaces has been a major area of research since the onset of high speed aviation. The interaction of shockwave with a boundary can be detrimental, since the adverse pressure gradient due to the shockwave/boundary layer interaction (SWBLI) causes the boundary layer separation. The boundary layer separation leads to reduction of efficiency and increment in the unsteadiness of the flow.

Perhaps it can be said that, the initial study of SWBLI dates back to 1939, when Ferri observed the SWBLI during testing of an airfoil in wind tunnel experiments. Wherein, the flow on the airfoil, accelerated from near sonic velocities to supersonic speeds, which then terminated in the form of quasi-normal shock. This was the case on curved bodies, but later on, the research area got concentrated on purely supersonic boundary layer, in which the pressure gradients were only due to the induced shock wave. Thus with the help of selected geometries, the effects on the shock strength, Mach number, Reynolds number on the flow field were systematically identified. Various scenarios where in a shock boundary layer interaction can be seen are described below.

1.2 Types of shock boundary layer interactions:

2D Compression Corner

In a 2D compression corner, a stabilized viscous flow approaches an inclined ramp of angle α . The ramp compresses the flow creating an oblique shock and turns the flow to follow the ramp surface. The increased pressure across the shock generates an adverse pressure gradient on the approach boundary layer, which drives the boundary layer towards separation. The pressure increase may also create an area of separation, which would result in a λ -shock. Based on the relative simplicity of this model, much work has been done to derive equations to describe the flow field behavior. This structure, while a relatively simple shape, has many real-world applications, the most common being shock cones and ramps associated with hypersonic vehicle engine inlets.

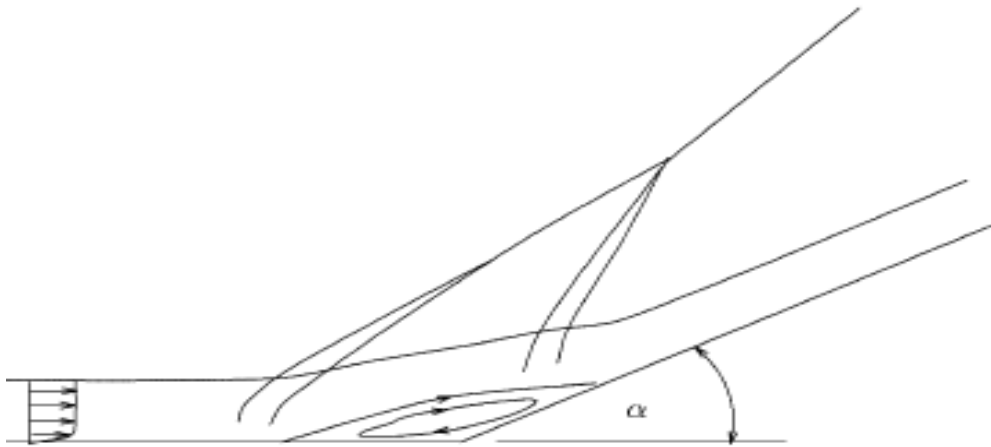


Figure 1.1: 2D Compression Corner

Shock Impingement

In a shock impingement, an incoming oblique shockwave intersects with a boundary layer developing on a wall. Even in supersonic flows, flow at the surface of a wall attains zero

velocity due to the no-slip condition and velocities very near the wall are still subsonic. When the increased pressure across the shockwave interacts with the slow speeds near the wall, an adverse pressure gradient region near the wall is created which makes the boundary layer prone to separation. When that separating boundary layer reattaches downstream, it forms a separation bubble. Further downstream, the boundary layer and reflected shock continue to interact, generating a complex flow field.

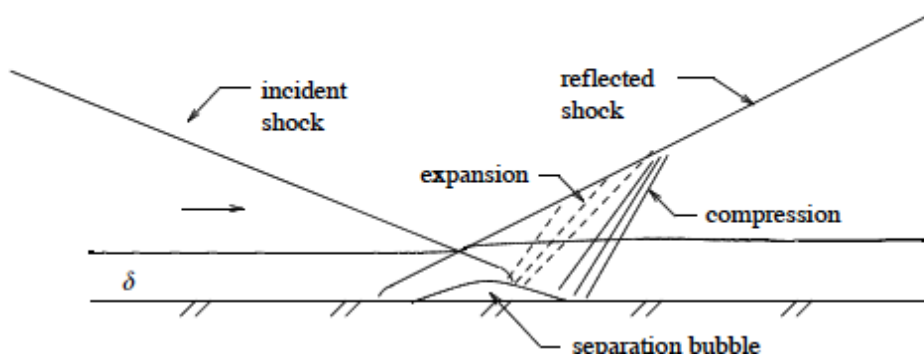


Figure 1.2: Shock Impingement

2D Expansion-Compression Corner

In a 2-D expansion-compression corner, supersonic flow experiences effects roughly opposite of a compression corner as the flow is allowed to expand naturally with a favorable pressure gradient. The flow expands and accelerates as it turns the corner, in accordance with the Prandtl-Meyer theory. With this acceleration, the density and pressure decrease, Mach number increases and the boundary layer becomes thicker. An additional effect of the favorable pressure gradient is the reduction of turbulence in the flow. In fact, the turbulence may even decrease enough to relaminarize the flow. As a result, the shear stress and heat transfer rate along the wall also decreases. Downstream of the initial expansion corner, the flow then turns back to its initial direction, compressing the flow once again and creating a shock that interacts with the boundary layer.

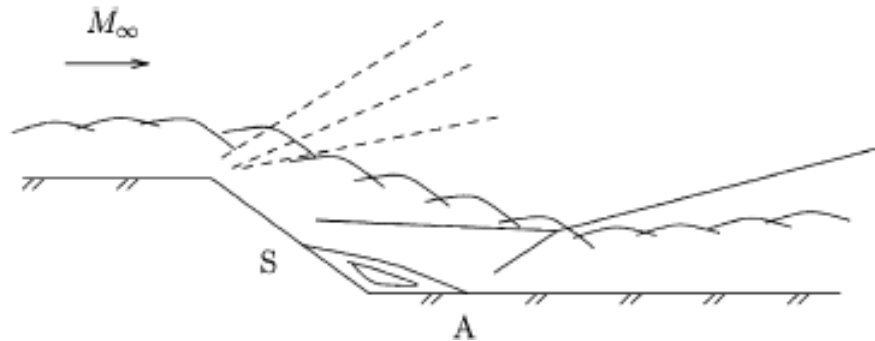


Figure 1.3: 2D Expansion-Compression Corner

3D Single Fin

In a 3D single fin configuration, a semi-infinite fin is attached at a 90-degree angle to a flat plate. The post-shock pressure increase is diffused along the length of the fin and the pressure variation along the fin follows a “quasi-conical” vortex pattern, in which the secondary cross flow skews the approach boundary layer in a manner that characteristically distinguishes it from 2D flow.

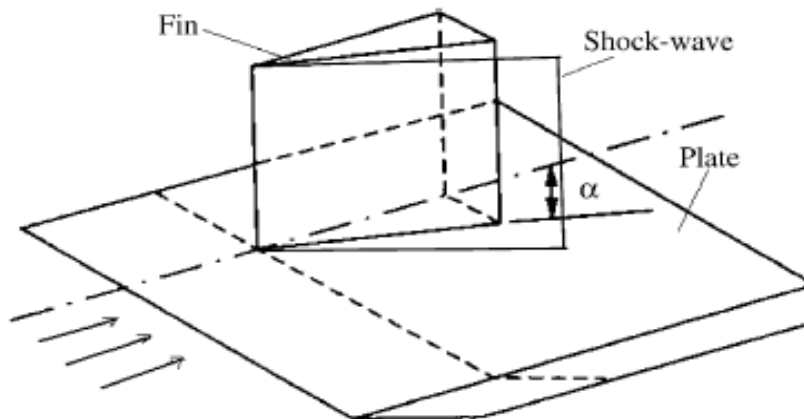


Figure 1.4: 3D Single Fin

3D Double Fin

The 3D double fin configuration represents the utmost complexity in basic models of SWBLI. In this model, all factors from the previous cases are combined into one problem. In the 3D double fin model, two semi-infinite fins are attached to a flat plate in close proximity.

Parameters of the model that can be varied are the two fin angles, the width of the entrance, the width of the throat, and the offset of the midpoint of the throat relative to the midpoint of the entrance. The resulting interactions are a combination of shocks, expansions, 3D effects, impingements, vortices, and multitudes of other complexities. This model has obvious implications for ramjet/scramjet inlets and is the newest and least understood model. The majority of information about this particular flow model comes from numerical computations, verified by some experimental data and images. The flow structure is extremely complex, composed of several regions of distinct but interaction flows.

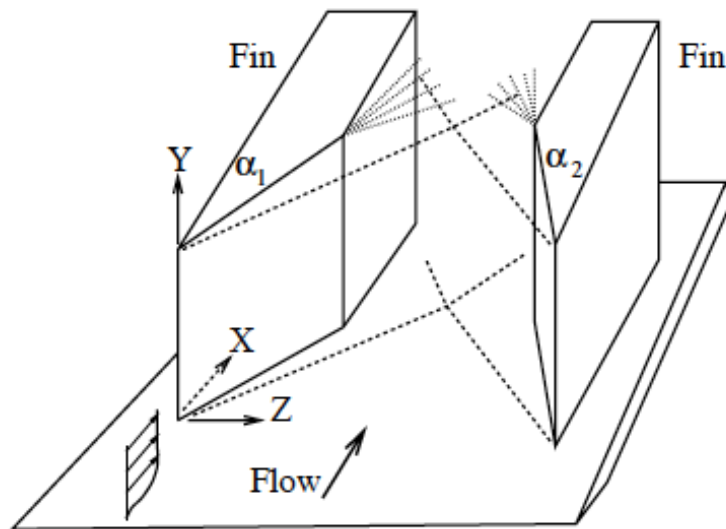


Figure 1.5: 3D Double Fin

The previous models present a baseline for understanding the complexities of SWBLI and allow a standard method for developing new methods of verifying CFD codes compared to real world interactions. Thus the models are the building blocks for understanding the complex phenomena involved. Even with all the complex flow fields involved in these models, particularly the 3D models, there are even more complex issues that arise when these models are studied over a period of time as opposed to the time-averaged results. These time-dependent

studies reveal an element of unsteadiness, which will be discussed in the next section, along with a historical cross-section of experimental and analytical studies in the field of SWBLI.

Considering the disadvantages of the SWBLI several control techniques have been proposed.

The research in the control is still an open research area. A few control techniques are described below.

1.3 Control Techniques

Controlling and/or eliminating the effects of the SWBLI are considered to be the next important focus of research. Flow control techniques have also been given high importance as, in general sense the outcomes can be applied for increment in efficiency and minimization of losses in desired systems.

Active Control: Lately, active control techniques have been given prominence, in which external source of power or energy is utilized in the flow field. Predetermined, interactive methods are two categories that active control techniques can be divided into. Steady or unsteady energy is input without considering the state of the flow field. Utilization of methods such as jet vectoring with the help of piezoelectric actuators done by Smith and Glezer (1997), form drag reduction with oscillatory blowing technique done by Seifert and Pack (1999) are some of the notable examples in active control.

Passive Control: Passive control methods have been used in considerable number of experiments. Passive control does not need external energy expenditure but needs changes in geometries such that it affects the pressure gradients. Vortex generators that are used for separation control and for drag reduction, grooves or riblets that are used on a surface are examples of such passive flow control devices. More detail about the passive flow control

techniques can be found in books by Kral (1999), Bushnell and Hefner (1990) and Gad-el-Hak et al. (1998).

The succeeding sections talk about the motivation for the current research, experimental setup, the analysis procedure and results and discussions.

CHAPTER 2

LITERATURE REVIEW

Current research is based on the shock impingement method where in the corresponding SWBLI is studied. As explained in the introduction section, an oblique shock wave interacts with the turbulent boundary layer and reflects back leaving behind a complex flow structure. The focus of this research which is to identify the inherent frequencies of the complex flow structure and also to identify the dominant flow using rainbow color schlieren technique and snapshot proper orthogonal decomposition, has been deduced by referring to the following previous research done in the area of shock wave boundary layer interaction with respect to shock impingement.

Initial research on SWBLI can be dated back to 1939, when Ferri first observed the SWBLI during tests on an airfoil in wind tunnel experiments (Ferri, 1939). Wherein, the flow on the airfoil, accelerated from near sonic velocities to supersonic speeds, which then terminated in the form of quasi-normal shock. This was the case of curved bodies, but later on, the research area got concentrated on purely supersonic boundary layer, in which the pressure gradients were only from the induced shock wave. Thus with the help of focused geometries, the effects on the shock strength, Mach number, Reynolds number were identified. Since then the study of the shock wave boundary layer interaction has been evolving from simple configurations to understand the structure of interaction to complex configurations to establish the flow physics in the turbulence.

In case of an inlet or on a transonic airfoil, the interaction between the boundary layer and the inviscid outer layer flow can cause significant changes in the flow structure (Delery, Dussauge, 2009). The basics of major types of interactions, such as oblique shock interaction

with the boundary layer forming on a surface, flow at a compression ramp, normal shock wave boundary layer interaction have been discussed by Jean Delery, Jean-Paul Dussauge (Delery, Dussauge, 1985, 2009). Review conducted by Dolling (Dolling, 2001), widely considered to be one of the most comprehensive of such reviews, covered the study in SWBLI over the past five decades. Various aspects of the boundary layer interaction that had been reviewed in his paper include the flow structure, heat transfer, flow field unsteadiness, the effects of the interactions and flow control. The study of the boundary layer interactions has been covered in both two dimensions as well as three dimensions. Importance has been given to the factors such as base-line applicability, simplicity, specific applicability, consistency, adequate data with respect to spatial and turbulence, test conditions and flow condition such that these factors can be incorporated in computational studies of the shock wave boundary layer analysis (Settles, Dodson, 1994).

Pirozzoli and Grasso (2006) have used direct numerical simulation codes to study the unsteadiness of the SWBLI on a flow at $M = 2.25$ with an impinging oblique shock wave with shock angle of 33.2° . The work was focused on determining the characteristic low frequencies of large oscillations. In which it was observed that due to the vortex-shedding near separation point, together with downstream propagation of the vortical structures in the mixing layer, generation of feedback pressure waves due to shock interaction at the foot of impinging shock, and upstream propagation of acoustic frequencies of cavity tones, caused the low-frequency unsteadiness. Adding to the understanding of SWBLI unsteadiness, Dussauge et al (2006) conducted a review of the phenomenon by evaluating various experiments, in particular the case of a shock reflection using varying plate angles of incidence from 7° to 9.5° with an incoming free stream flow of Mach 2.3. It was determined that the frequency of the fluctuations produced

by the shock motion is much lower than the characteristic frequencies of turbulence present in the incoming boundary layers. The shockwave itself apparently acted as a sort of low pass filter, which selected only the lower frequency excitation. It was suggested that in the shock impingement-reflection scenario the three-dimensional separation bubble may be at the origin of the unsteadiness caused by the shock boundary layer interactions. The Strouhal number is defined as dimensionless shock frequency can be obtained as $S_L = (f_s L)/U_e$, where f_s is the characteristic shock frequency, L is the length of interaction and U_e is the external velocity. In this case they considered the ratio of length of oscillation L_{ex} , (length pertaining to the unsteady reflected shock which is deduced from longitudinal evolution of standard deviation values of wall pressure fluctuations) and to the length of interaction L , to study the Strouhal number. The ratios considered were in the range of 0.3 – 0.5. The Strouhal number which was obtained for the experiments was in the range of 0.03 - 0.05 provided the order of magnitude of the dominant frequencies and gave meaningful trends. It was also interpreted that the source of excitation of the shock was due to the eddies in the separated zone. Another interpretation was that the shock wave itself acts as a low pass filter, and it would select only the low frequency part of the excitation.

It was observed that the flow reattaching downstream was based on the properties of the fluid entrainment in the mixing layer downstream of the separation shock (Piponniau et al, 2009) in case of shock impinging boundary layer analysis performed over a free stream Mach 2.3 on two wedges with angles 8° and 9.5° . Particle image Velocimetry was used to obtain the velocity fields. The low frequencies associated with the separation shock were found to be related to the successive contractions and dilatations of the separation bubble. The dominant frequencies of 384Hz and 171Hz obtained for the 8° and 9.5° configuration were close to the theoretical

calculations. The incoming velocities behind the separation shock were 505m/s and 490 m/s respectively. The Strouhal number $S_L = (f \cdot L)/U$, where f is dominant frequency, L is the length of interaction and U is the velocity behind the separation shock, thus calculated was in the range of 0.025 – 0.05, which was in accordance with the values obtained in experiments conducted by Erenkil and Dolling (1991), Dolling and Brusniak (1989) and Wu, Martin (2008) with different configurations.

It has been observed that on an instantaneous basis, the interaction region exhibits a multi-layered structure, characterized by a relatively high-velocity outer region and low-velocity inner region (Humble et al, 2009). The experiments were conducted in a free stream Mach number $M = 2.1$, with an oblique shock generator of deflection angle 8° . The discrete vortical structures which are prevalent along their interface were identified to create an intermittent fluid exchange as they propagate downstream. Proper orthogonal decomposition results suggested that the instantaneous fullness of the incoming boundary layer velocity profile was weakly correlated with the size of the separation bubble and the position of the reflected shock wave. To obtain the Strouhal number they had used the length of interaction of 45mm and free stream velocity of 518m/s. Thus the Strouhal number calculated in this experiment was in the range of 0.1 – 0.27 which was about 3 – 10 times larger than the most energetic Strouhal numbers reported elsewhere, which were in the range of 0.02 – 0.05. This discrepancy which is currently an active research, has been studied further in the experiment and quantity L_{rms} which is the root mean square of the instantaneous separation bubble length was considered to calculate the Strouhal number. Upon using the r.m.s value the Strouhal number resulted in the range of 0.01 – 0.03 which was much better in agreement with others. However it was identified that the reflected shock region was dominated by the low frequencies which are of lower in order of magnitude

compared with the frequencies in the undisturbed boundary layer at the same distance from the wall. The eigen modes returned from POD showed an energetic association between the velocity fluctuations within the incoming boundary layer, separated flow region and across the reflected shock wave. The modes portrayed subspace features that represented to an extent the phenomenology observed in the instantaneous realizations.

Dussauge and Piponnier (2008) have analyzed the possible sources of the unsteadiness in the shock boundary layer interactions using the results from multiple experiments majorly concentrating on the shock impinging concept. It was observed that when a shock wave interacted with a boundary layer without inducing separation, the shock motion was dominated by the structure of inflow turbulence. It was speculated that the three dimensional vortices formed in case of the 9.5° had a circulation of the order of the dominant frequency of the shock motion. However in case of 8° wedge angle, there were no three-dimensional eddies, but there were significant motions at low frequencies. It was assessed that there may not be any particular flow structure with appropriate frequency scale to date. In some subsonic separated zones, modes of Kelvin – Helmholtz type were developed, producing beating at low frequency. It was interpreted that if such models can be applied to turbulent supersonic separation, it could constitute a rather convincing theory to explain the low frequency shock motion.

Range of frequencies and the space scales present in the flow, together with three dimensional structure of the separated flow has been studied in a free stream Mach number of $M = 2.3$ with an oblique shock generator at 8° and 9.5° (Dupont et al, 2005). It has been observed that unsteady reflected shock upstream of the interaction zone moved with very low frequencies and the reflected shock moves at a very low average speed of a few meters per second, which suggested that the synchronization of the fluctuations and the formation of eddies through the

shock motion is unlikely. Presence of the low frequencies was accounted to be up to 25% to the total energy of the pressure fluctuations. The level of the reverse flow was about 15% in case of 9.5° wedge angle, for which a strong modification of the flow was found; where in three-dimensional organization of the flow was observed. It was concluded that further work needs to be done to relate the low-frequencies of the reflected shock and the time scale of the large three-dimensional scales in the separated region.

Visualization of the flow fields associated with the shock wave boundary layer interaction has been majorly done by schlieren methods (Kleine and Groenig, 1991). These methods are widely used for visualization of the shock structure, using the refractive index variations in a transparent media. It becomes hard to interpret from the black and white pictures if the flow field tends to be complex. Recognizing the flow patterns of high turbulent flow becomes more difficult. Hence, with the utilization of the color schlieren technique, as used in the current work, determining the turbulent boundary layer, impinging-reflecting shock, the separation bubble and expansion region can be investigated more clearly.

In the color schlieren method, there is a direct correspondence between the hue of the flow field and the index-of-refraction obtained in the same flow field. The index-of-refraction changes due to the temperature variation in the flow. Density of the flow field varies accompanying the temperature variation and the species concentration in general. In general, the densities across the test section changes during the run time, the deflections of hue values are recorded using a high speed camera (Albers and Agrawal, 1999). Hiromu Sugiyama et al (2006) used the color schlieren method to find the pressure fluctuations, wall shear stress distributions for pseudo shock waves generated at Mach 2 and Mach 4, in a square duct of $80 \times 80 \text{ mm}^2$ cross

section. The wall shear stress distribution in the Mach 4 pseudo-shock wave region was investigated by shear-sensitive liquid crystal coatings. All the regions in the SWBLI structure, such as the interaction between the impinging shock and the turbulent boundary layer, separation, and reattachment were clearly identified.

Snapshot Proper Orthogonal Decomposition is one of the major statistical techniques utilized in the identification of the dominant structures in a flow field. The essential features of the flow field i.e., the energetic motions can be identified by the combination of the desired orders of the POD modes (Yang et al, 2009). For the purpose of turbulent flow characterization Proper Orthogonal Decomposition has been employed with either numerical or experimental data (Hilberg et al, 1994). Identification of large scale coherent structures in turbulent flows has been studied by Gurka, Liberzon and Hetsroni (2006). Particle Image Velocimetry (PIV) data has been used to obtain the span wise vorticity. Snapshot POD has been applied in identifying the dominant flow structures and flow dynamics in chemical process by Tabib and Joshi (2008). The data collected from PIV and Large Eddy Simulation (LES) has been used to obtain the dominant spatial topology of the velocity and vorticity structures. The structural length scales were obtained using the image processing on spatial modes. Using PIV velocity and unsteady wall pressure measurements in a Mach 2.3 flow and an oblique shock generator with a deflection angle of 9.5° , Piponniau et al (2011) have identified the spatial-time correlation between wall pressure and velocity in a shock wave turbulent boundary layer interaction. POD and Linear Stochastic Estimation (LSE) have been used for the analysis of the space-time correlation. This helped in predicting the unsteady aspect of the recirculating bubble.

CHAPTER 3
EXPERIMENTAL SETUP

3.1 Wind Tunnel

The schematic drawing of the wind tunnel can be seen in Figure 1. The wind tunnel comprises of compressors, driers, storage tank, pressure regulator, stagnation chamber, nozzle, test section, wedge and diffuser. The description of each part is as follows.

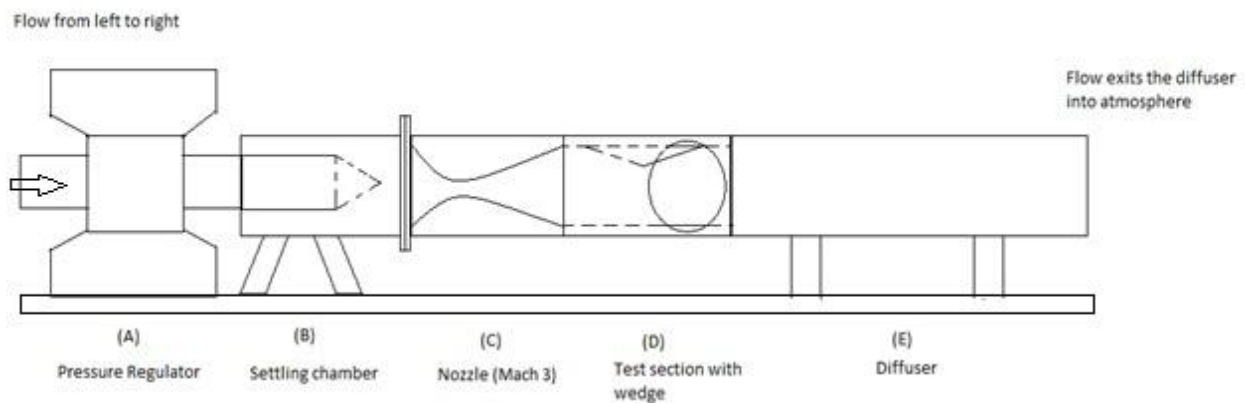


Figure 3.1: Schematic drawing of the wind tunnel

3.1.1 Storage Tank and Compressors:

A storage tank of 0.5inch thick wall and a volume of 28 m³, with a maximum allowable design pressure of 1.38 MPa (200 psia) were used for the air supply purpose. Two, Ingersoll – Rand compressors of model SSR – HXP50SE with a capacity of 170 CFM were used to supply the compressed air to the storage tank. The compressors rated operating pressure is 185 psig. A 3 phase, 60 Hz, 50 hp motor was used to run each of the compressors. For the purpose of drying the air, an automatic air-cooled Ingersoll – Rand dryer, model TZ300HP-EMS-3V-LDP was used. The desiccant used in the dryers was activated alumina with dew point of -73⁰C/ -100⁰F.

For the experimental purpose the storage tank pressure was taken up to 140 psi at where the experiment was run. Following figures 3.2 and 3.3 show the dryers and compressors used.



Figure 3.2: Dryers



Figure 3.3: Compressors

3.1.2 Pressure regulator and stagnation chamber:

Wind tunnel's operating pressure was regulated by a 3 inch LESLIE pressure regulator. A butterfly valve was used to control the air flow from the storage tank to the pressure regulator. Compressed air of 140 psi is reduced to 65 psi using the pressure regulator for the experimental purpose. As flow passes the pressure regulator, it enters the stagnation chamber. The stagnation chamber contains a flow straightener, damping screen and a pitot probe. The flow straightener was made up of 4 inch long 0.5 inch in diameter steel tubes. A perforated cone and a damping screen were used as metal jackets for the tubes at the downstream and upstream respectively.

3.1.3 Nozzle and test section:

A Mach 3 aluminum nozzle manufactured at UA was used as the nozzle. The nozzle is 25.4cm in length with a throat area of $1.65 \times 7.62 \text{ cm}^2$. The inlet area of the nozzle is $15.24 \times 7.62 \text{ cm}^2$ and the exit area of the nozzle was $7.62 \times 7.62 \text{ cm}^2$. A test section of dimensions $7.62 \times 7.62 \times 30.5 \text{ cm}^3$ that was also manufactured at The University of Alabama, Tuscaloosa is attached to the end of the nozzle to form the test section of the tunnel. The side walls of the test section contained circular flat optical glass to view the flow field and to obtain the flow images. The test section floor was made up of solid optical grade plexiglass. A wedge of 12° was bolted to the ceiling of the test section to get the desired oblique shock. Dimensions of the wedge used were $11.95 \times 7.62 \text{ cm}^2$ and 1.27cm thick at the center. The wedge is placed at a certain distance on the ceiling, such that the desired oblique shock impinges at the required portion of the test section, such that the interaction region can be captured from the glass windows, using the rainbow color schlieren technique.

SolidWorks cut section views for both the wind tunnel assembly and test section alone can be seen below in the figures. The figures depict the arrangement of the wedge and the circular glass window in the test section.

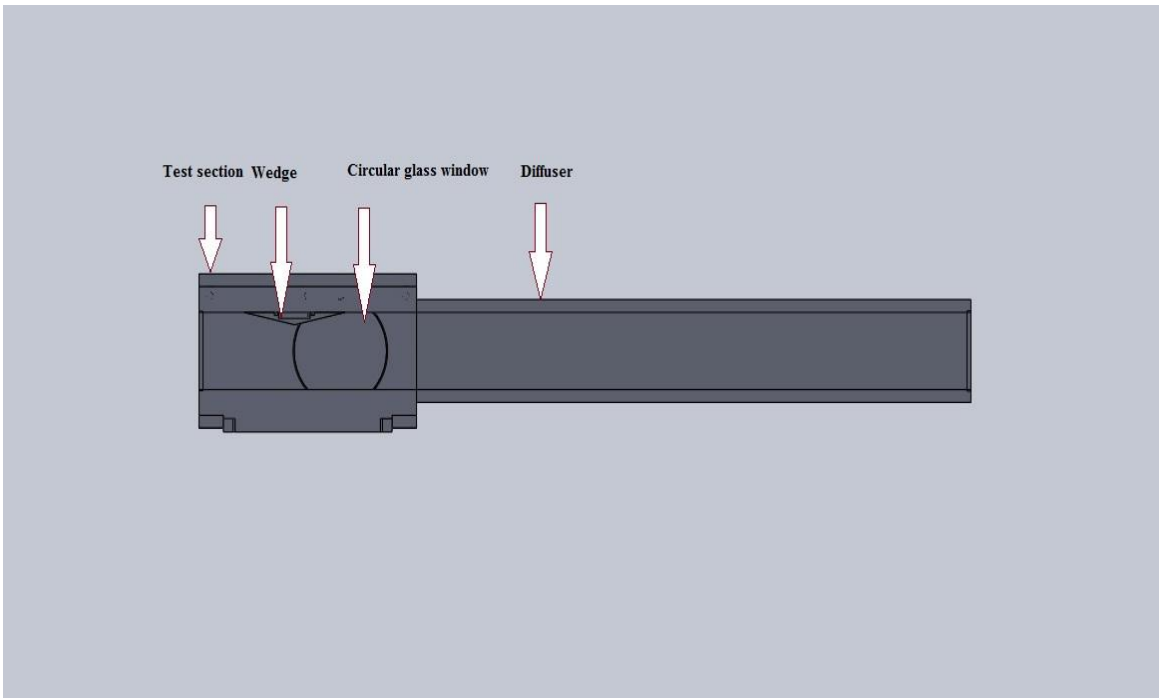


Figure 3.4 SolidWorks cut section view of the test section and diffuser assembly

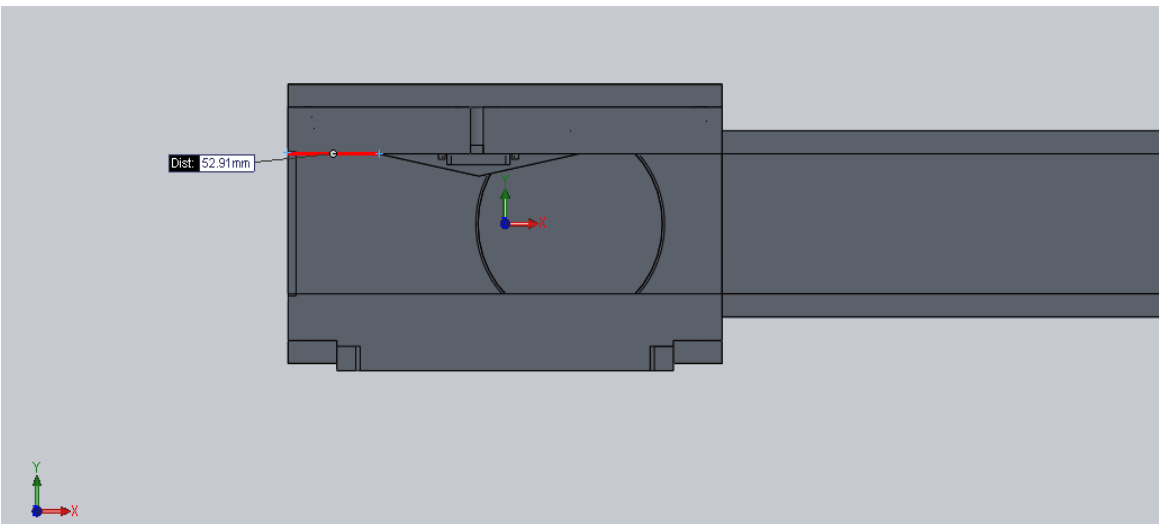


Figure 3.5 SolidWorks cut section view of the test section

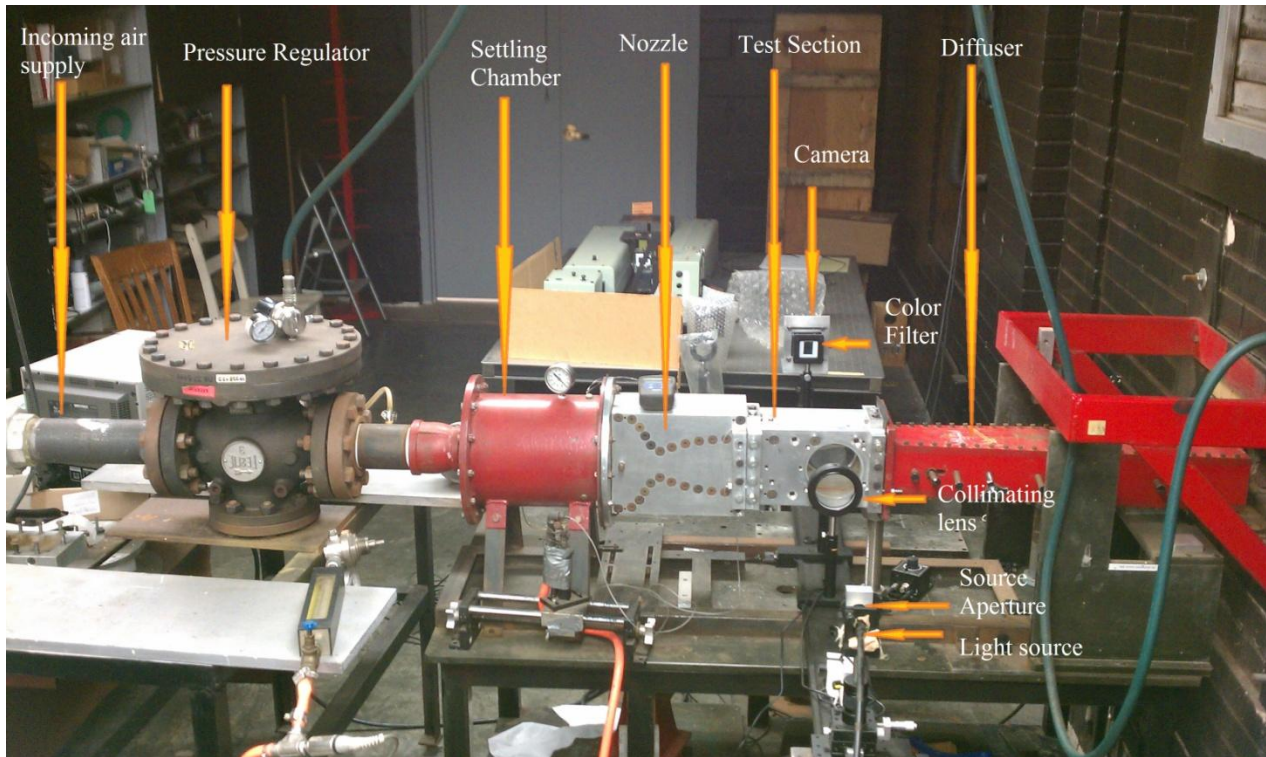


Figure 3.6 Actual setting of the wind tunnel assembly

3.1.4 Diffuser:

A variable area supersonic diffuser was used to operate over a range of Mach 1.5 to Mach 4.0. The walls of the diffuser consisted of a hinged plate which could be adjusted with the Mach number of the test section. In the current research, a 63.5 cm long diffuser with an inlet area of 7.62 cm x 7.62 cm and the outlet area 12.7 cm x 7.62 cm was used.

3.2 Color Schlieren Apparatus

The shockwave boundary layer interaction occurring in the test section was captured using the color schlieren apparatus. The Figure 5 shows the schematics of the apparatus. The light source used in the experiment was TECHNIQUIP – FOI- 250 fiber optic illuminator, which had a halogen lamp mounted inside. A 200- μm -wide aperture was placed in front of the

fiber optic light source, through which light diverges and hits the collimating lens.

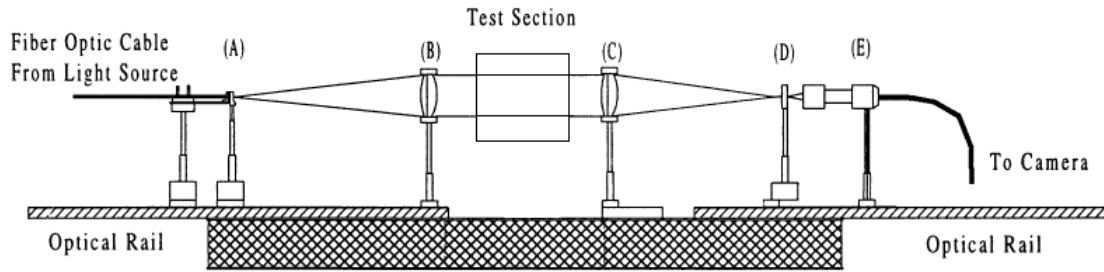


Figure 3.7: Schematic of Color Schlieren Apparatus

Where (A) is Source Aperture, (B) is collimating lens, (C) is decollimating lens, (D) is Rainbow Filter, (E) is High speed camera.

Light from the source was collimated by achromatic lenses of 76.2mm diameter, 500 mm focal length and decollimated by 76.2 mm diameter, 750 mm focal length. Actual picture of the apparatus can be seen in figure 3.8. Rainbow color schlieren filter was a 35 mm slide with a 3mm wide asymmetric strip of continuously varying colors, which can be seen in Figure 3.9.

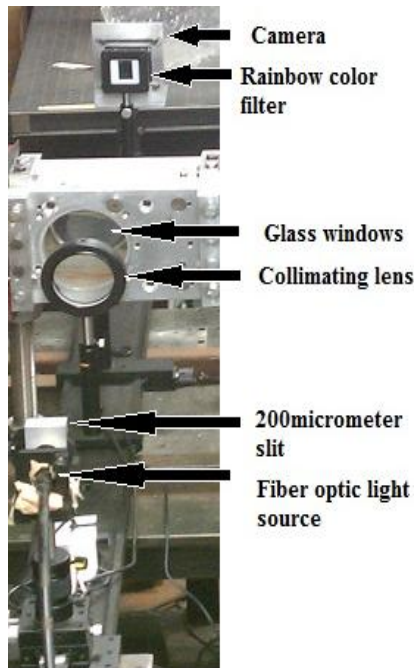


Figure 3.8 Actual setting of the color schlieren apparatus



Figure 3.9 Color filter

The filter used in the experiment is an asymmetric filter with hue varying from 199° to 104.7° and then to 249.7° and to 197.8° . The initial dip from 199° to 104.7° and final dip from 249.7° to 197.8° in the hue variation is due to the gradual transition of colors on the filter from adjacent dark region into the colored region and transition from the colored region exiting into the dark region. Hence only the linear portion of the hue variation which is 104.7° to 249.7° is considered for the analysis purpose. Asymmetric filter has its advantage over the symmetric filter, since in the asymmetric filter the colors vary from red to blue. And hence we can obtain positive and negative gradients without redundancy. Whereas in symmetric filter the colors vary from red to blue and then again from blue to red, which gives double color variations for positive as well as negative deflections. Hence to avoid redundancy in positive and negative deflections an asymmetric filter has been used in our case.

The filter is continuously graded and hence it transmits the light of particular wavelength corresponding to the location on the filter. This helps in calculation of the lateral displacement of light rays at the filter plane corresponding to each pixel location in the color schlieren image.

The camera used was HGTX – Imager, model 2000 from ROPER scientific. The camera requires a DC power supply to operate. The DC power supply used in the work was HY3003 D-3, which produces an output of 1.4A, 24V that is required for running the camera. Sony Trinitron color video monitor was used for the purpose of visualizing the images.

The color schlieren images were acquired at a rate of 1000 frames per second by the camera, at an exposure rate of $23\mu\text{s}$. The digitized images were stored as 384 x 512 pixel files in Tag Image File Format (TIFF). The system provided a data acquisition rate of 1000 Hz as each image frame was composed of two fields taken 1/1000 second apart. The field of view was

concentrated at the side of the test section where the glass windows are located so that the SWBLI could be observed.

CHAPTER 4

ANALYSIS PROCEDURE

4.1 Color Schlieren Analysis

Rainbow color schlieren technique uses a continuously graded color filter as explained in the experimental setup section. The rainbow filter is used to observe the transverse displacements of the light rays. Colors vary in the filter in an asymmetric manner, varying from red to blue along the filter. The image obtained through this would be in RGB format. RGB format contains the Red, Green and Blue color values of the image. In an RGB format for each pixel there would be three parameters varying, which leads to excessive computing during the image processing. Hence the images are converted to HSV/HSI format, which is Hue, Saturation and Value/Intensity format. In Hue Saturation Intensity (HSI) color model, the colors can be characterized by using just the Hue value. The color spectrum is divided between 0 to 360 degrees range with 0 and 360 corresponding to red, and 180 degree corresponding to cyan. While the Saturation and the Intensity give the grey content in the color and the brightness of the color respectively, they do not contribute in defining the color.

The slit at the light source and the color filter are placed horizontally such that they are parallel to the ground. This has been done so as to capture the deflections of light in the vertical direction with respect to the filter. The deflections were more pronounced in this position. Images were also taken with the slit and filter kept in perpendicular to the ground, to capture the deflections in horizontal direction. Key information in the images, such as the boundary layer, clarity in the separation bubble region was missing when experiment was run in this fashion as the deflections were majorly in vertical direction. The color filter has to be calibrated based on the hue variation along the filter. For the purpose of calibration, the rainbow color filter is

traversed from edge to edge in increments of $50\mu\text{m}$ and simultaneously images are captured at each location without the flow in the test medium. A MATLAB code has been written which calculates the average hue value for each image and compares with the background image to obtain the calibration. Figure 4.1 shows calibration curve corresponding to the color filter used.

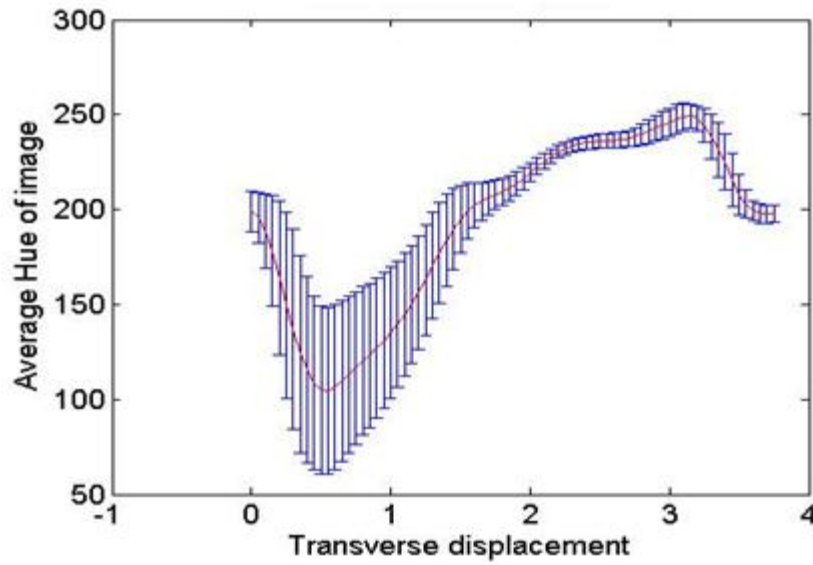


Figure 4.1 Filter Calibration Curve

As seen from the figure 4.1, the hue varies from 199° to 104.7° and then to 249.7° and to 197.8° . The initial dip from 199° to 104.7° in the hue variation is due to the gradual transition of colors on the filter from adjacent dark region into the colored region and final dip from 249.7° to 197.8° is due to the transition from the colored region on the filter into the dark region on the filter respectively. Hence only the linear portion of the hue variation which is 104.7° to 249.7° is considered for the analysis purpose so that there would not be any redundancy in hue identification. The refined hue versus distance curve can be seen in the figure 4.2.

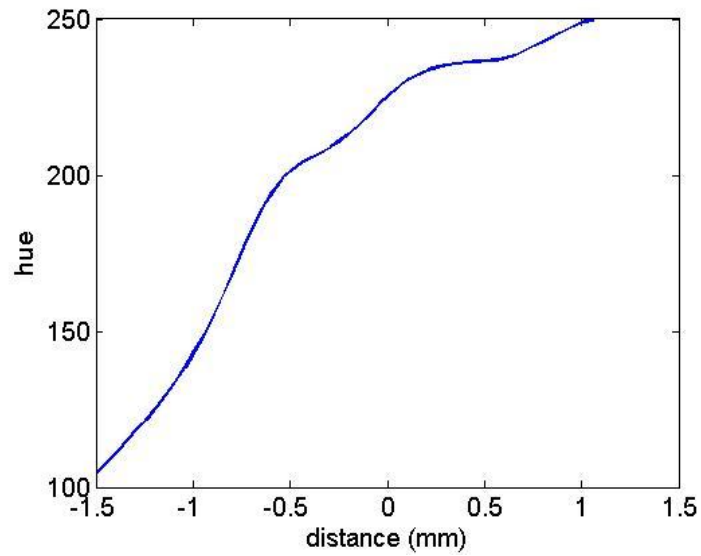


Figure 4.2 Refined Calibration curve

The color schlieren images are acquired with and without the flow without disturbing the optical setup, hence a given pixel, maps to particular physical location in presence or in absence of the flow. This is the reason that it is not desirable to move any part of the apparatus during the actual run. The calibration curve depicts the range of hue values that vary across the color filter. A background image is taken keeping the light source focused at a desired color on the filter without flow in the tunnel. In the current experiment light is focused at the dark blue portion of the filter to get the background image.

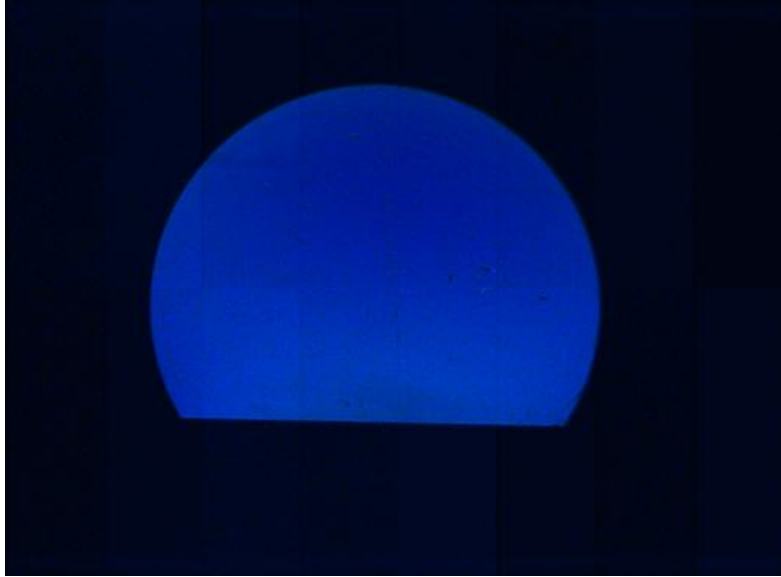


Figure 4.3 Background image

Figure 4.3 shows the background image for the current experiment. The image is cropped such that only the colored portion of the image is considered to calculate the average hue value.

During the tunnel run, HGTX-Imager camera is used to capture the images at 1000 frames per second rate at $23\mu\text{s}$ exposure time. A total of 2730 images can be captured in a single run due to the memory limitations of the camera. These images are transferred from the cache of the camera to the computer on which the analysis of these images is done. A MATLAB program is written for the purpose of the analysis of these images. The program compares the calibration curve and the background image's hue value and gets the zero shift position. Later, the test images are read.

As explained earlier, MATLAB originally reads the images in the form of Red Green Blue (RGB) color format, which is converted to HSV color format for the purpose of current work.

The test images are obtained at 384 x 512 pixel resolution. The following Figure 4.4

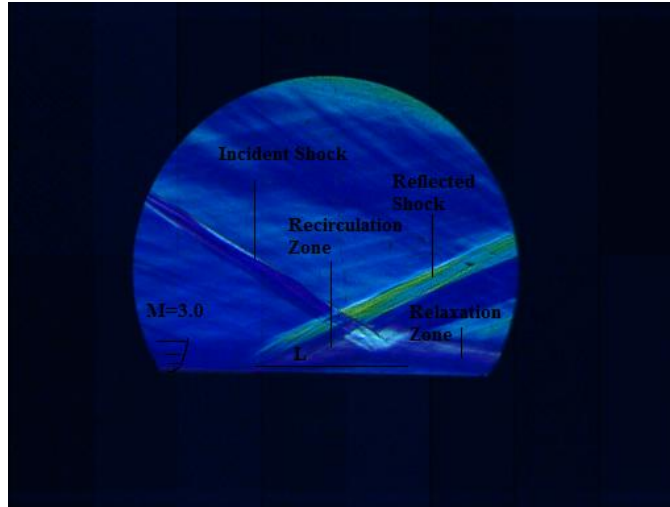


Figure 4.4 Test image

displays the test image. The images are then cropped to 223 x 294 pixel resolution such that the images display the desired test section portion, there by neglecting the unnecessary portion. The

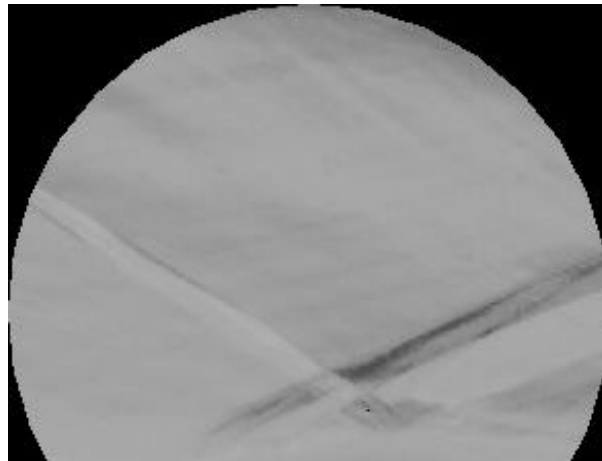


Figure 4.5 Cropped Image

cropped image can be seen in above figure. Using the zero shift value and the hue values of the test images, the deflections are calculated. The transverse ray displacement at the filter plane is given by:

$$d = f_c * \varepsilon$$

Where f_c is the focal length and ε is the deflection angle, d is the deflection determined by the hue of the image at a pixel location. The transverse ray displacement is proportional to the

difference between the local hue value of the test run image and hue value of the background image.

The angular deflection of a light beam for a two-dimensional flow is given by:

$$\varepsilon = \left(\frac{L}{n_o} \right) \frac{\partial n}{\partial x} |Q$$

where L is the width of the test section, n_o is refractive index of air, n is refractive index of air in the test section at a point Q, x is the coordinate axis perpendicular to the optical path. For air, the relationship between the refractive index and gas density is given by:

$$n - 1 = k\rho$$

Where k is Gladstone-Dale constant, which is $k=0.23 \text{ cm}^3/\text{g}$ for air and ρ is density of the air. Hence using the refractive index and density relations, one can obtain the density gradient as follows:

$$\frac{\partial \rho}{\partial x} |Q = (d(1 + k\rho_o))/(Lk f_c) \approx d/Lk f_c$$

Where n_o is taken 1, since for air, refractive index is 1. For the initial boundary conditions, the density is calculated using perfect gas equation.

$$\rho = P/RT$$

Where P is the pressure, R is specific gas constant and T is temperature. Once the density of the flow is known, say along a line, through the boundary conditions, then one can use the density gradient values and calculate the density in the flow by stepwise integration.

The transverse ray displacements obtained at every pixel of each of the pictures were then used to calculate the ensemble average and the standard deviation of the displacement values at every pixel location using all the pictures taken during the experiments as:

$$\overline{d_{i,j}} = \frac{\sum_{n=1}^{N_t} d_{i,j}}{N_t}$$

Where $\overline{d_{i,j}}$ denotes the ensemble average deflection at the pixel location given with the (i, j) indices, and N_t is the number of successive pictures used in the calculation. Each image was made up of 384 X 512 pixels, thus i index varied as $i=1, \dots, 223$, and j index varied as, $j=1, \dots, 294$. The standard deviation of the displacement at each pixel location was calculated using:

$$\sigma_{i,j} = \sqrt{\frac{1}{(N_t - 1)} \left(\sum_{n=1}^{N_t} (d_{i,j} - \overline{d_{i,j}})^2 \right)}$$

4.2 Fourier Transform

The transverse ray displacement values were also used to calculate the frequency content of the displacements. Time dependent deflection values obtained at a pixel position using sequential pictures was used to calculate the Fourier transform of the signal at every pixel point separately. The FFT data was then used to calculate the power spectrum at every pixel location. The power spectrum thus obtained at every pixel location was then used to determine a) the frequency at which the spectrum shows a peak and, b) the power contained at a certain frequency at that pixel location (discussed in results and discussion part). Once the results of the FFT analysis was obtained at every pixel location one then could generate a figure of these variations for the whole view. The frequencies across the image varied from 1 to 500 Hz since the data was taken at a 1000 frames/s rate. During the analysis the DC component of the data was neglected to determine the dominant frequencies in different regions of the flow. This analysis was aimed to determine if different regions of the flow fluctuated with preferred frequencies.

Power spectrum displayed pixel-wise power values, for a given frequency. Further in the discussion section, the variation of power in the flow field has been discussed at selected frequencies. Strouhal number which is a dimensionless shock frequency is defined based on the power spectrum and the frequency analysis. Strouhal number $S_L = f*L/U$, where f is the

dominant frequency, L is the length of interaction and U is the free stream velocity. Here the dominant frequency can be identified from the power spectrum values. The dominant frequency is the value that corresponds to the maximum values of the power spectrum values near the foot of the shock and in the recirculation region close to the wall. The length of interaction L is defined as the length in between the point on the wall from the extrapolated incident shock and the reflected shock. As the reflected shock does not originate at a single point in every frame of the flow, the length is calculated from each point of origination of the reflected shock which extends into the approach boundary layer and to the point of extrapolation of the incident shock and an average is taken on the all the lengths taken to give the length of interaction on the whole. A MATLAB code has been written for the same purpose to identify the length of interaction. After the length of interaction L is obtained and the dominant frequency or the dominant frequency range is obtained, Strouhal number can be obtained by $S_L = f^*L/U$.

4.3 Snapshot Proper Orthogonal Decomposition

The pictures of the transverse ray displacement obtained using the color schlieren technique was used as the input data for the snapshot POD analysis. Each picture with its 223 x 294 pixels formed the 2-D field at time t_n , and is referred as a snapshot. The total number of snapshots is denoted with N_t . Each snapshot had $n_1 \times n_2$ (223 x 294) data points. A time correlation tensor is obtained using these pictures given with the following equation:

$$[R]_{ij} = \frac{1}{n_1 n_2} \sum_{l=1}^{n_1} * \sum_{m=1}^{n_2} H(X_{lm}, t_i) H(X_{lm}, t_j)$$

Where n_1 and n_2 indicate the number of grid points in the x and y coordinate axes respectively. In this equation, H denotes the deflections matrix. X denotes the coordinate

variables. Using Fredholm equation POD coefficients are found with relation to the correlation matrix.

$$RA^{(n)} = \lambda^n A^n$$

$$A^n = |a^n(t_1), a^n(t_2), \dots, a^n(t_{N_t})|$$

Where A^n is the eigenvector matrix built up from the POD coefficients a^n , λ^n denotes the n^{th} eigenvalue and corresponds to the energy contained within the n^{th} eigenmode. The amount of the total energy associated with the flow field could be represented by the sum of λ^n as follows:

$$E = \sum_{n=1}^N \lambda^{(n)}$$

where N is the number of eigenmodes. The POD mode is then obtained by projecting the original flow fields onto their corresponding coefficient as follows:

$$\Phi^{(n)}(X) = \sum_{k=1}^{N_t} a^{(n)}(t_k) H(X, t_k)$$

All the POD modes are orthogonal and hence the reconstruction of any member of flow field can be possible as follows:

$$H(X, t_k) = \sum_{n=1}^N a^{(n)}(t_k) \Phi^{(n)}(X)$$

Among all the modes, the most energetic mode represents the dominant pattern of the flow field. Hence, all the large scale structures can be obtained by adding the low energy modes. The highest energy mode can be obtained by truncating the full series of the eigenmodes to a desired order, assuming a descending order of the eigenvalues,

$$\hat{H}(X, t_k) = \sum_{n=1}^K a^{(n)}(t_k) \Phi^{(n)}(X)$$

CHAPTER 5

RESULTS AND DISCUSSION

This chapter presents the results obtained from the color schlieren image processing, Fourier transform and snapshot proper orthogonal decomposition. A MATLAB code has been written to perform image processing, ensemble averaging, Fourier transform and Snapshot Proper Orthogonal Decomposition. Section 5.1 explains the results from ensemble averaging. Section 5.2 explains the results from Fourier transform and describes how the frequencies play the role in the shock motion and unsteadiness. Section 5.3 explains the results obtained from the Snapshot Proper Orthogonal Decomposition and subsequently explains the flow structure of the corresponding modes.

5.1 Color Schlieren results

As explained in the analysis section, based on the calibration curve and the background image the test images are read by the program to calculate the deflections. The pixel wise deflections are plotted in the form of a contour as shown below in Figure 5.1.

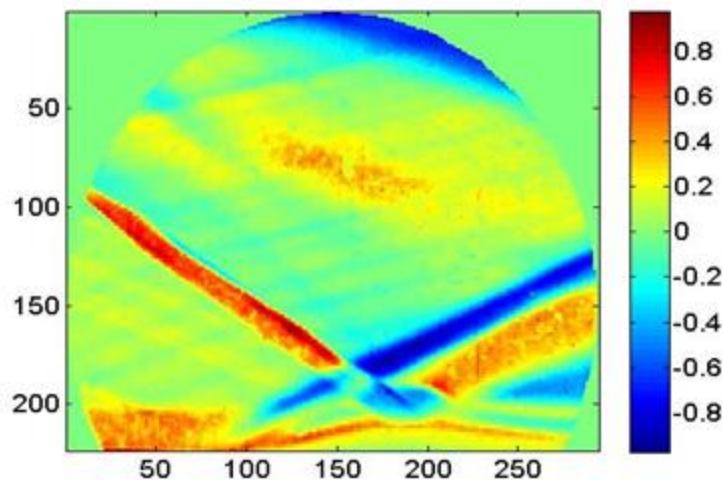


Figure 5.1 Ensemble average deflection lengths

The following figure 5.2 explains the detailed sections of the flow configuration observed with the ensemble averaged deflections.

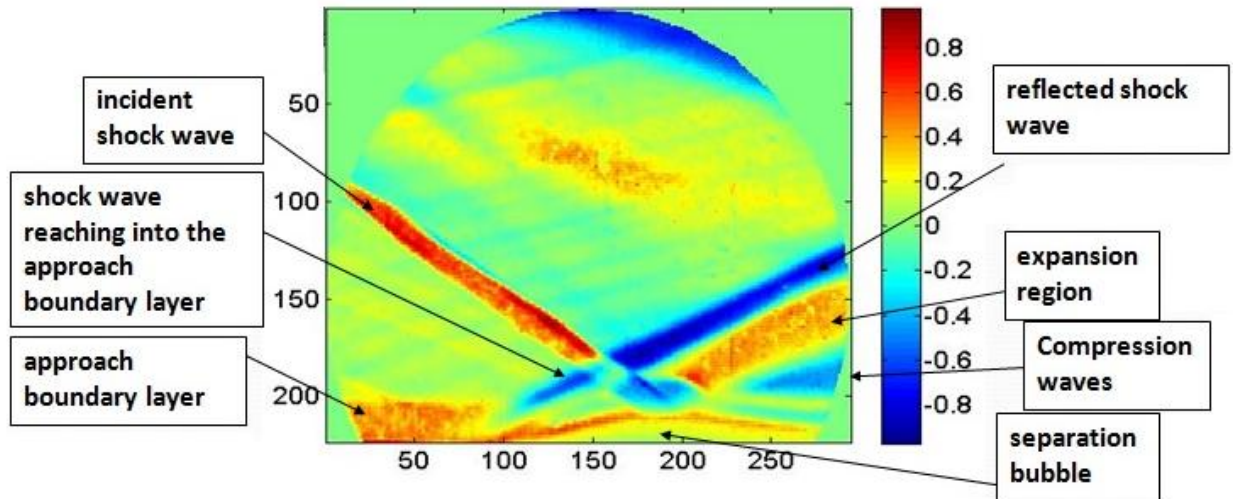


Figure 5.2 Detailed flow structure of the shock boundary layer interaction

Deflections as obtained above display the hue variations in the parts of the image where the shock boundary layer interaction is prominent. Detailed explanation of various regions in the shock wave boundary layer interaction is explained in the following paragraphs.

Impinging shock and the incoming boundary layer:

From the image, the incoming turbulent boundary layer, the impinging shock, point of interaction in between these two, area of separation, reflected shock, lambda shock formation, expansion region, re-attachment shock structures can be clearly identified. The deflections are seen higher in the impinging shock and the reflected shock as it is known that there would be considerable amount of density change across the shock. It can also be seen that there is a considerable change in the density across the expansion region as well where in the deflections change from negative values to positive values. It can be observed that in the separation bubble, the deflections were close to zero, as that part of the flow is subsonic.

Recirculation zone:

The impinging shock wave causes pressure and density variations across the shock wave. The increased pressure behind the impinging shock wave is imposed on the boundary layer behind the shock wave. The pressure jump generated by the shock wave results in an adverse pressure gradient on the boundary layer. The near wall flow with the low momentum flow rate affected by the pressure gradient separates from the floor. The flow field beneath the shock wave experiences a flow reversal and the tip of the separation region extends upstream of the impinging shock wave's expected intersection location with the wall. It is observed that the existence of low frequencies in this region may also play a vital role in the flow mechanism in the separation bubble. It was mentioned by Piponniau et al (2009) that the reversal of the flow in this region is because of the entrainment of flow caused by eddies at the foot of the reflected shock. These generated eddies would shed into the downstream flow outside the separated region. And when the flow reattaches downstream the mass amount inside the bubble decreases and steady separated flow could not be maintained, which leads to the unsteady movement of the separation bubble and hence the flapping motion of the foot of the reflected shock was observed.

Relaxation zone:

The presence of the separation region results in disturbance in the boundary layer and results in a second shock generation. The interaction of the impinging shock and the shock generated due to the presence of the separated region intersect resulting in a shock/shock interaction flow field. Shock generated by the presence of the separation region extends and merges with the shock generated due to reflection. The extent of the impinging shock wave closer to the wall, the reflected shock, and the shockwave generated due to separation generates a complicated flow field downstream of the shock waves dominated by expansion and shock

waves. Separated flow reattaches with the relaxation of the pressures downstream of the shock waves thus leaving behind the separation bubble. It has been observed from the current experimental work using the frequency analysis that this region is primarily affected with a mix of medium and high frequencies. The frequencies and corresponding power involved in this region is covered in detail in Fourier transform results section.

Based on the hue deflections, the density gradients are obtained at each pixel location and are plotted in the form of a contour as shown in figure 5.3. Using the procedure mentioned in the analysis section, pixel-wise densities are calculated and plotted in the form of a contour as shown below in figure 5.4.

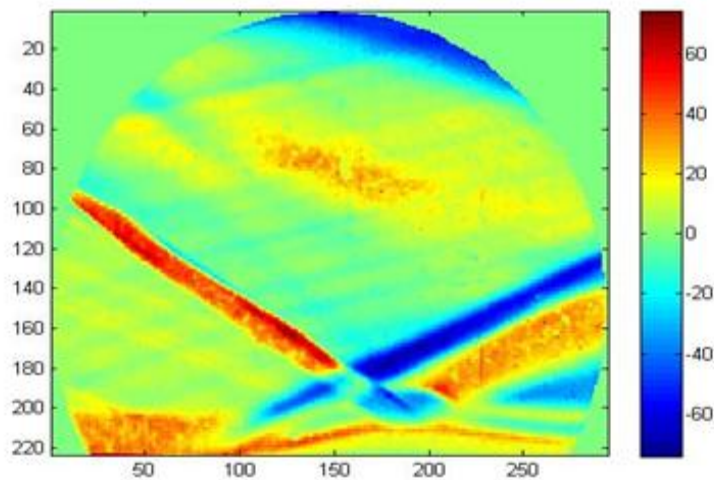


Figure 5.3 Average density gradients

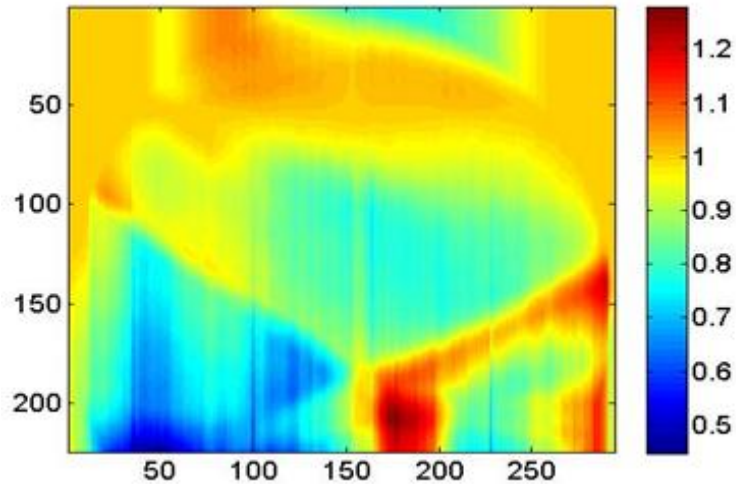


Figure 5.4 Average density

It can be seen from the figure 5.4 that, the density changes across the impinging and reflecting shock wave as well as in the area of the separation bubble were significant. It can be seen that the density increased from low to high across both the impinging and reflecting shock and also across the reattachment shock. The density has decreased in the region of the expansion, which is below the reflected shock. It has been observed that maximum average density was at the point of interaction of impinging and reflecting shock. The integration of the density gradients was performed from a chosen pixel location in the image. The hue values at the pixels that are out of the circular outline of the test data interfere during the integration process, which causes the density contour blotchy.

After calculating the ensemble average of the deflections and density, the same data has been used to calculate the Root Mean Square (RMS) values of the deflections and the density gradients. Figures 5.5 and 5.6 show the RMS values of the fluctuating displacements and also the density gradients of the hue at each pixel location over the entire images.

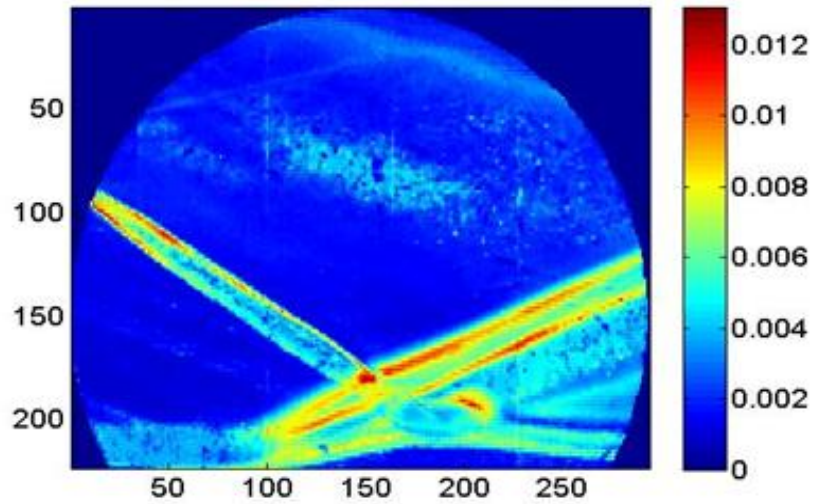


Figure 5.5 RMS fluctuating deflection lengths in mm

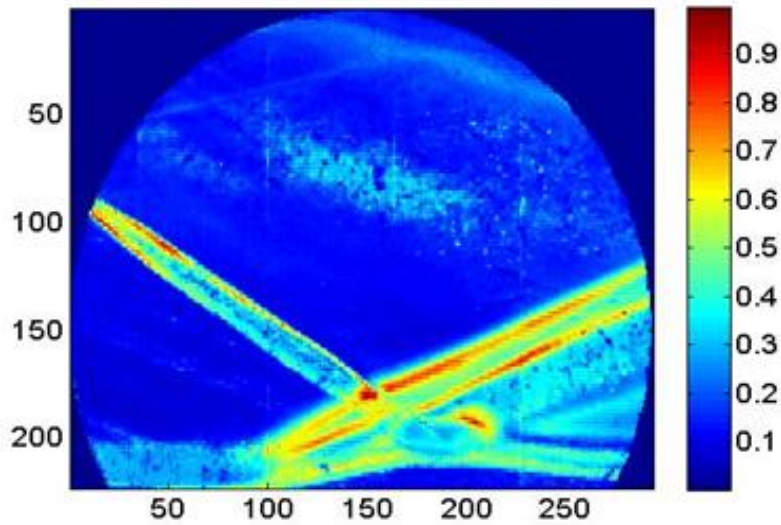


Figure 5.6 RMS fluctuating density gradients

The RMS values were seen to be higher at the interaction point of the impinging and reflected shock and in the recirculation zone and near the foot of the reflected shock which is the

part of the shock wave reaching into the approach boundary layer. It is also noted that the RMS values were higher in the region where the expansion fan originates downstream the separation bubble.

5.2 Fourier Transform results

The same data is used to calculate the frequency content of the density gradient fluctuations in the flow. Fast Fourier transform has been used to calculate the frequencies of the deflections at local positions. The subsequent images were used to determine the time-dependent deflections at a pixel position. Time dependent deflection values at a pixel position was then used to calculate the Fourier transform of the signal, to calculate the power spectrum of the signal. Power spectrum shows the distribution of the power as a function of frequency. The process was repeated at every pixel locations. The power spectrum of the signal at every pixel position was then used to determine a) the frequency at which the spectrum shows a peak, b) the power contained at a certain frequency at that pixel location. By calculation the values described in a), and b), at every pixel location one then could generate a figure picture of these variations for the whole view. The frequencies across the image varied from 1 to 500Hz when the number of samples used for analysis where 1024 images. The maximum frequency values where the spectra peaks are obtained are plotted as a contour plot in Figure 5.7 and Figure 5.8 below.

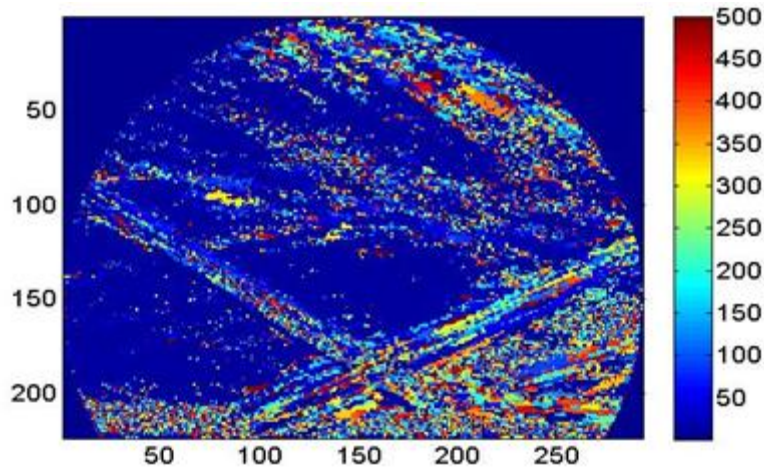


Figure 5.7 Pixel wise maximum frequencies

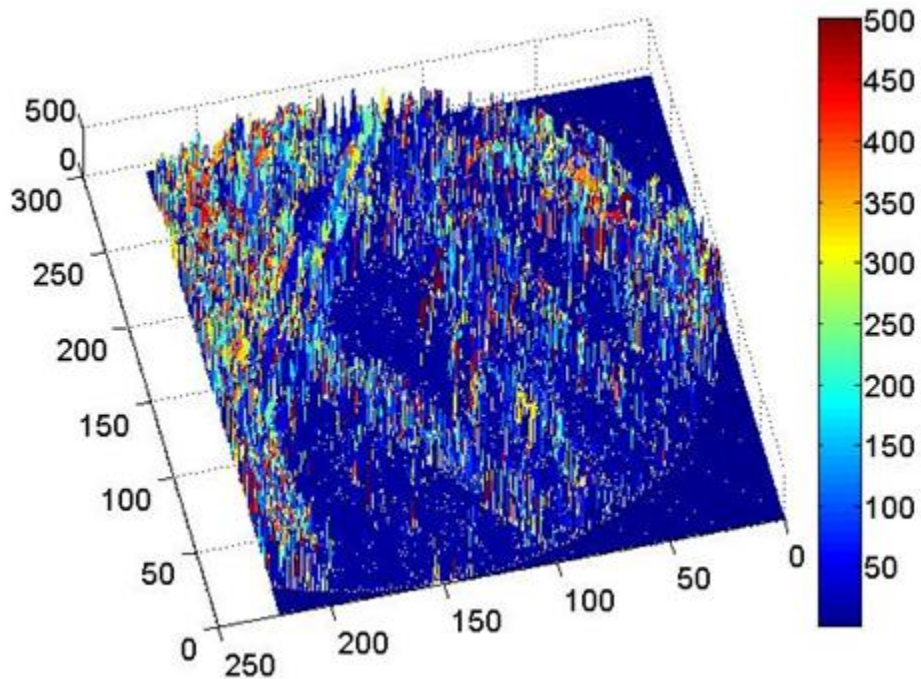


Figure 5.8 Pixel wise peak frequency distribution

It can be observed from the figure 5.7, that the fluctuations are more prominent in the downstream of the recirculation zone i.e. the separation bubble region, where the medium and high frequencies are present. The lower frequencies were more dominating in the recirculation region and just at the root of the reflecting shock. The frequencies which were dominant in the

recirculation zone were less than 50Hz. The nature of the shock motion at the foot of the reflected shock can be related to the low frequencies which are dominant in the relaxation zone, foot of the reflected shock and in the separation bubble but it is not clearly established. Pixel wise power spectrum for the entire 223 x 294 pixels are calculated and plotted in the form of a contour considering 1024 images. Individual power spectrum contours are considered for the frequencies ranging from 9.76Hz to 500Hz, such that the frequency range at which the maximum power spectrum occurs can be spotted. The description about the power spectrum values corresponding to the individual frequencies is as follows.

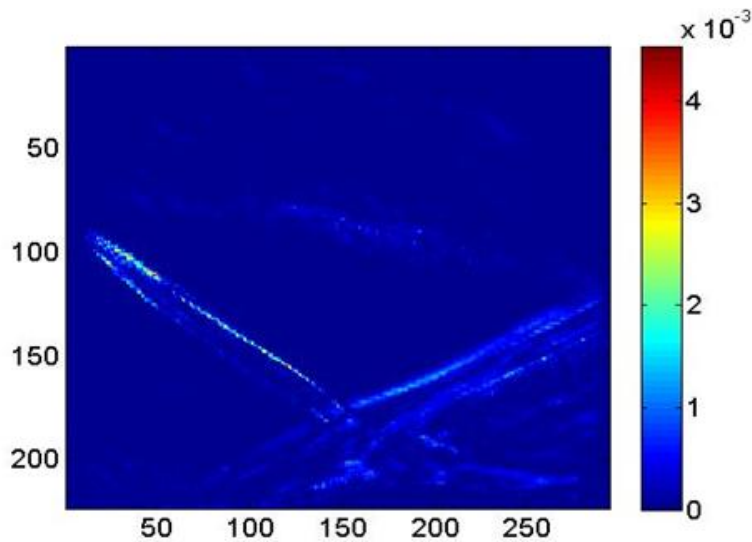


Figure 5.9 Power spectrum at 9.76 Hz

Figure 5.9 displays the power spectrum at the frequency of 9.76 Hz. At this frequency the power spectrum values are higher within the incident shock. The values in the interaction region, recirculation region, expansion region and in the separation bubble area are close to the minimum values. It can be deduced that at lower frequencies the power spectrum values in the recirculation and relaxation zone tends to be at lower end. The power values at the frequency of 14.65 Hz can be seen in the form of contour as below in Figure 5.10.

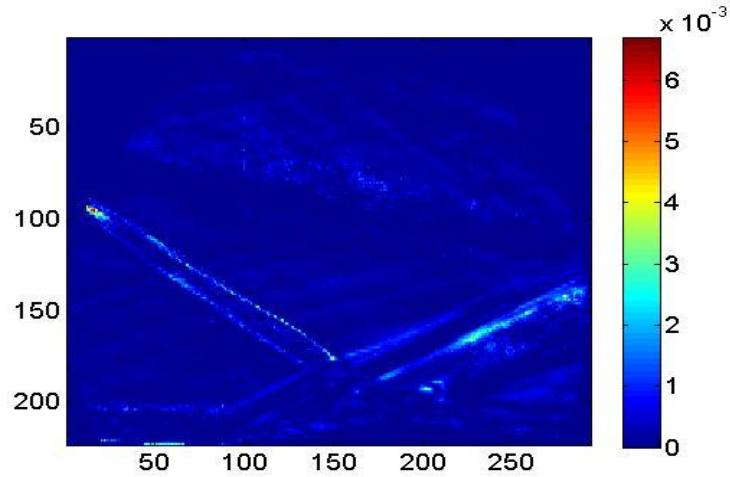


Figure 5.10 Power spectrum at 14.65 Hz

It has been identified that at this frequency the power spectrum values are relatively higher in the region of the reflected shock and near the foot of the expansion region. But the higher values still accumulated along the incident shock region.

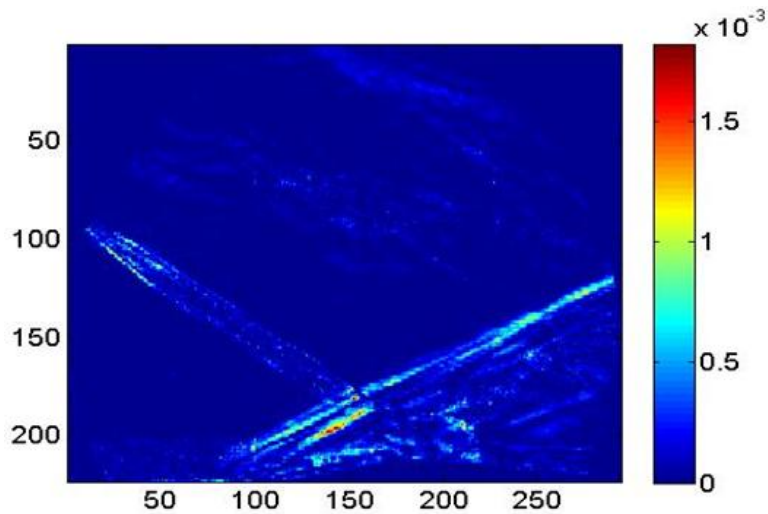


Figure 5.11 Power spectrum at 24.41 Hz

From the Figure 5.11 at the frequency of 24.41Hz, it is observed that the power spectrum values appeared to be higher in the comb like structure at the foot of the reflected shock. There is also a variation of power in the recirculation region, where in the power near the separation bubble is relatively higher compared to other low frequency power spectra in that region.

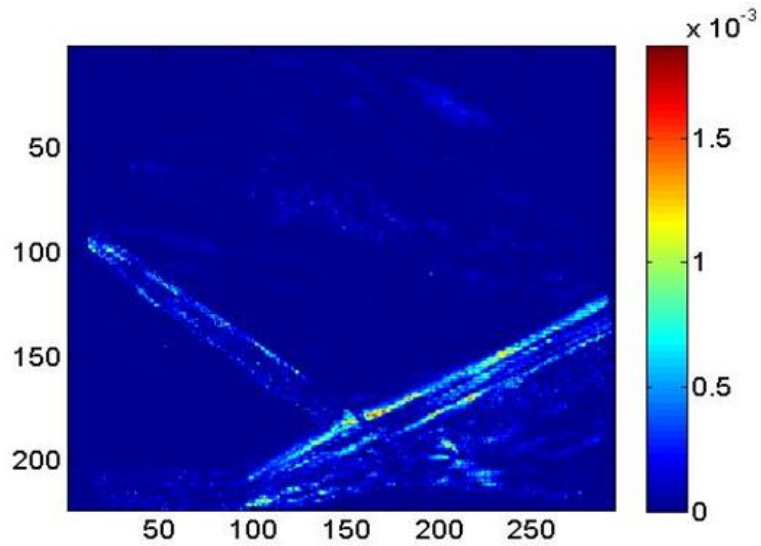


Figure 5.12 Power spectrum at 48.82 Hz

The higher values of power spectrum have shifted from the foot of the reflected shock which is observed in Figure 5.10 to the reflected shock as a whole as seen in Figure 5.12. The power distribution in this case clearly shows the difference in the power values just above the separation zone. The values in the separation zone fall towards minimum.

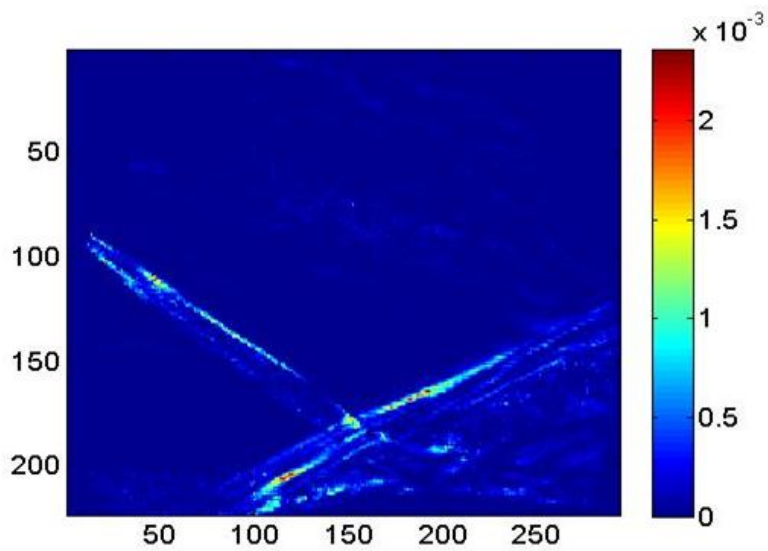


Figure 5.13 Power spectrum at 73.24 Hz

Figure 5.13 shows, higher values of the power are spread in the region of the foot of the reflected shock, reflected shock and relatively lower values in the incident shock. This change in distribution can also be seen in the subsequent frequencies.

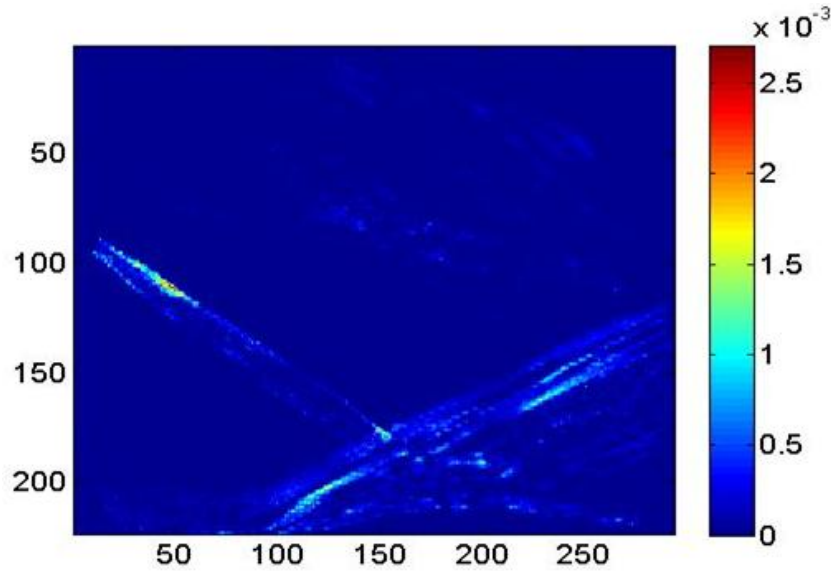


Figure 5.14 Power spectrum at 97.66 Hz

As seen from the earlier figures the power values tend to continue to be larger as the frequency increases. The power values at 97.66Hz (Figure 5.14) seem to be higher compared to the values at 73.24 Hz values, but the power distribution remained the same, i.e. higher values in the reflected shock wave and relatively lower values in the incident shock. It can be clearly seen that at both 73.24 Hz and at 97.66Hz there is no noticeable change in the power values in the separation bubble region.

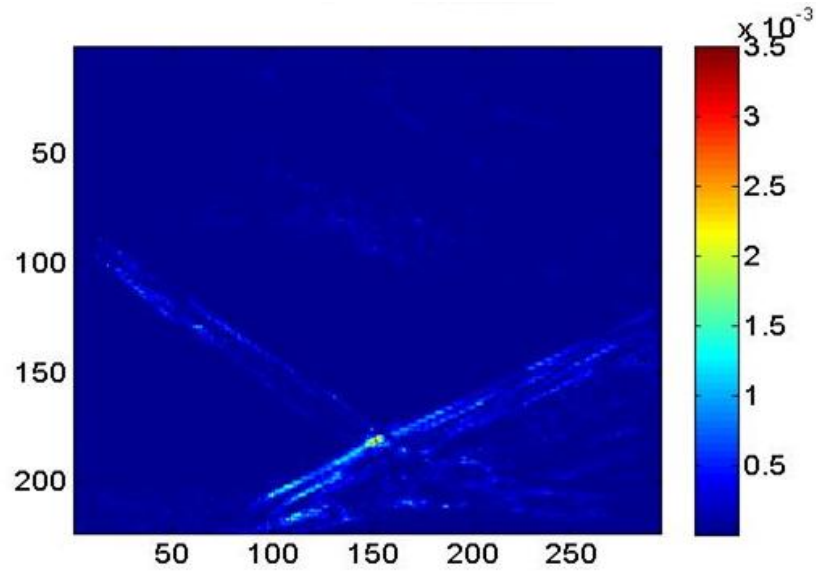


Figure 5.15 Power spectrum at 122.07 Hz

Figure 5.15 shows that at 122.07Hz higher power spectrum values were concentrated at the point of the intersection of the incident and the reflected shock. It has also been observed that the magnitude of power was relatively higher compared to the earlier frequencies. It is also noted that there is a shift in the values of power from the incident shock towards the recirculation zone.

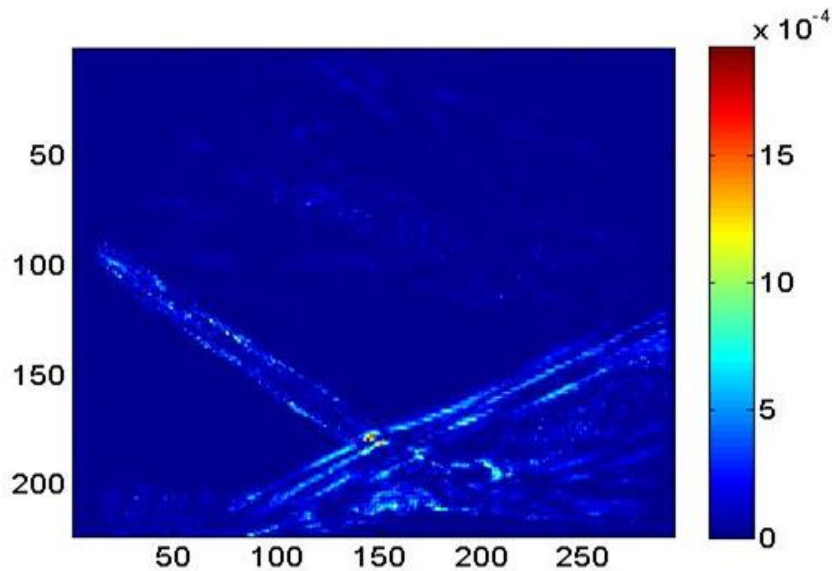


Figure 5.16 Power spectrum at 146.49 Hz

From the Figure 5.16, it can be seen that at 146.49 Hz the power peaks at the point of intersection of the incident shock and the boundary layer and the reflected shock. Apart from this, it is only in the recirculation zone, that there are considerable fluctuations that the power spectrum tends to be higher relative to the other regions.

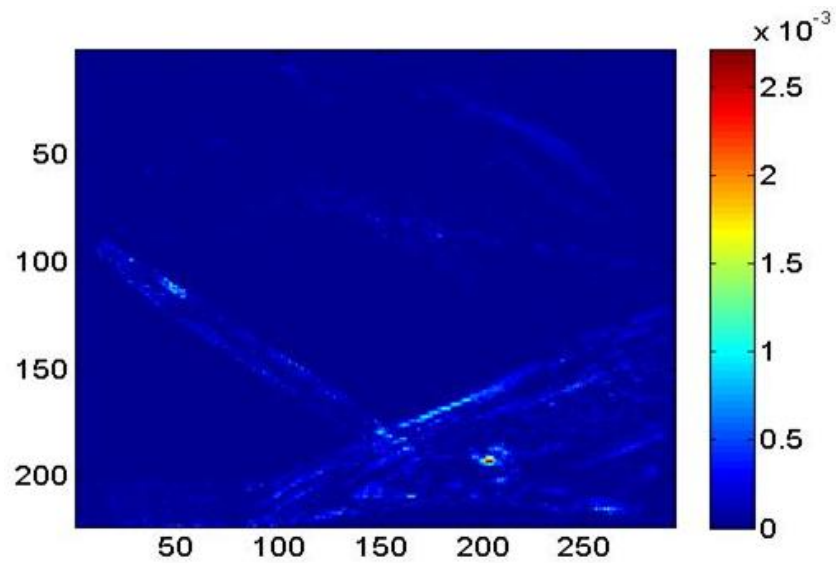


Figure 5.17 Power spectrum at 170.90 Hz

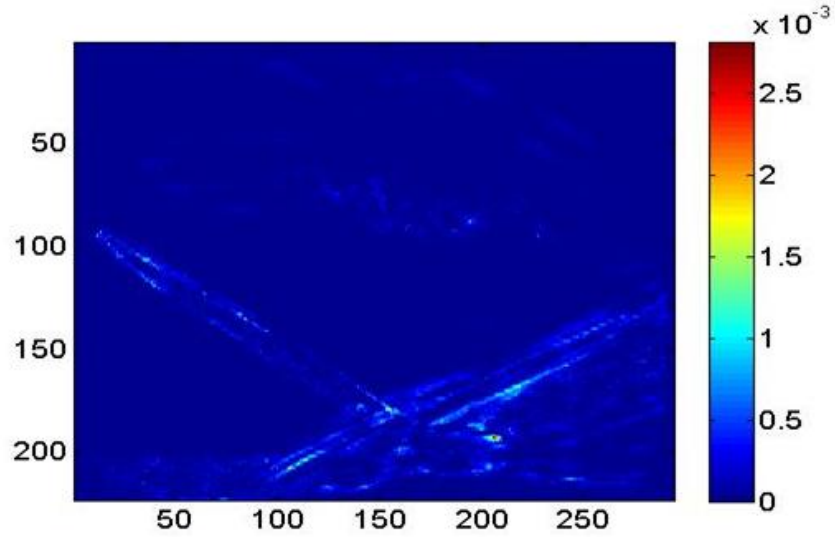


Figure 5.18 Power spectrum at 195.32 Hz

In Figures 5.17, 5.18 and 5.19 which are the power spectrum contours for 170.90Hz, 195.32Hz and 219.73Hz frequencies, peak power values were found to be at the foot of the expansion region and above the recirculation region. It can be inferred that it is at these frequencies that there are more density gradient fluctuations near the foot of the expansion region, which is effected by the recirculation region.

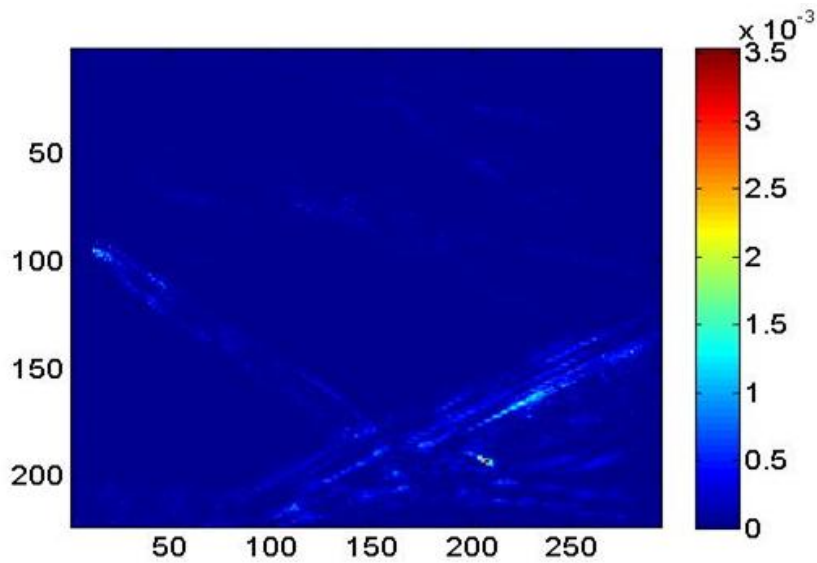


Figure 5.19 Power spectrum at 219.73 Hz

In the Figure 5.20 higher power spectral density values are spread over the reflected shock and the foot of the expansion regions, which is in the vicinity of the relaxation zone.

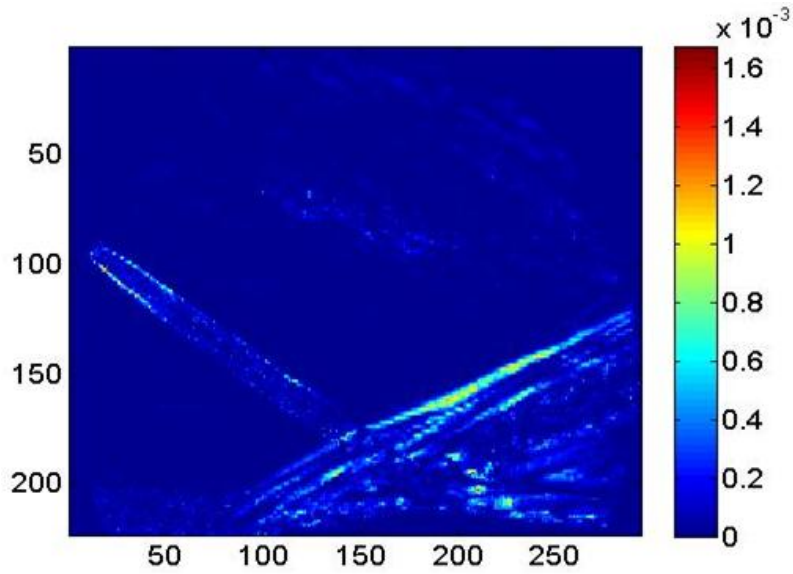


Figure 5.20 Power spectrum at 244.15 Hz

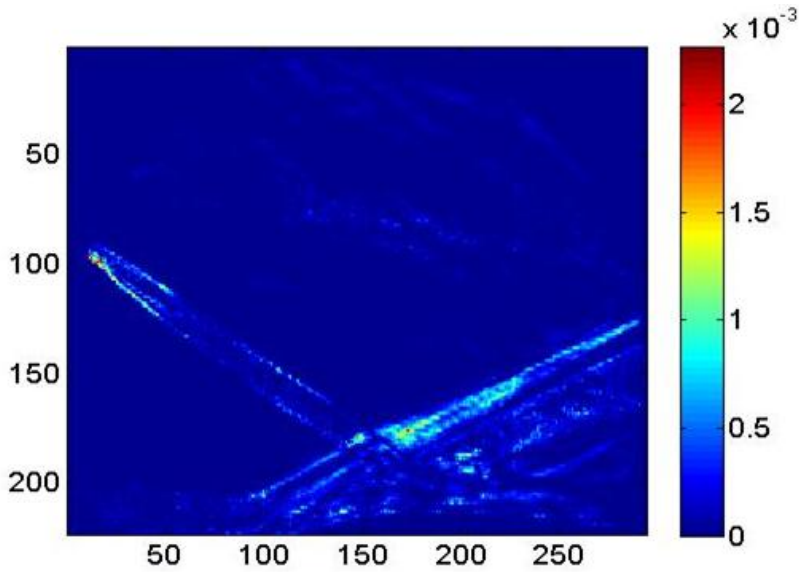


Figure 5.21 Power spectrum at 268.56 Hz

In the Figure 5.21, density gradient fluctuations were seen higher in the region of interaction and in the reflected shock, where as in the relaxation region, the deflections still

continue to affect the expansion region and the compression region downstream the separation bubble.

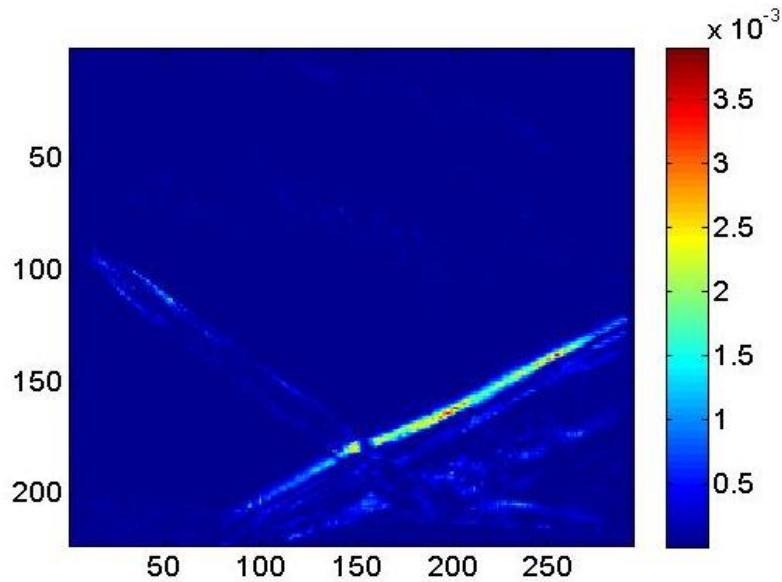


Figure 5.22 Power spectrum at 292.98 Hz

At the frequency of 292.98Hz from Figure 5.22, it has been noted that the higher power values are shifted on to the reflected shock wave. However, it is also observed that the recirculation zone and relaxation zone experienced relatively higher power values compared to the earlier frequencies.

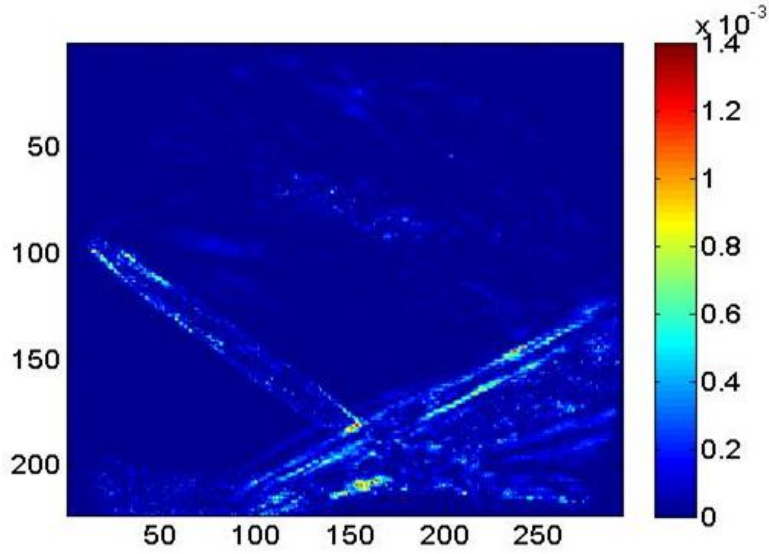


Figure 5.23 Power spectrum at 317.39 Hz

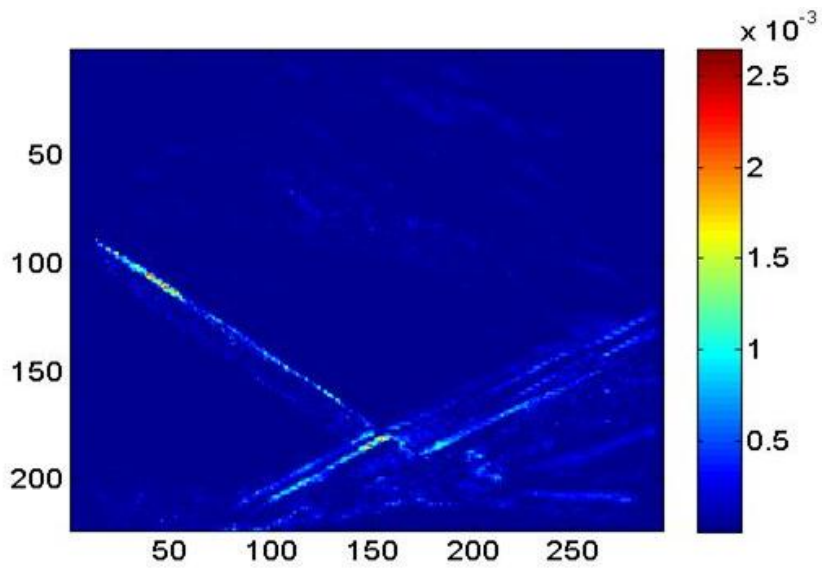


Figure 5.24 Power spectrum at 341.81 Hz

Figures 5.23 and 5.24 show that, higher power spectrum values were seen to be concentrated in the region of incident shock and the foot of the reflected shock.

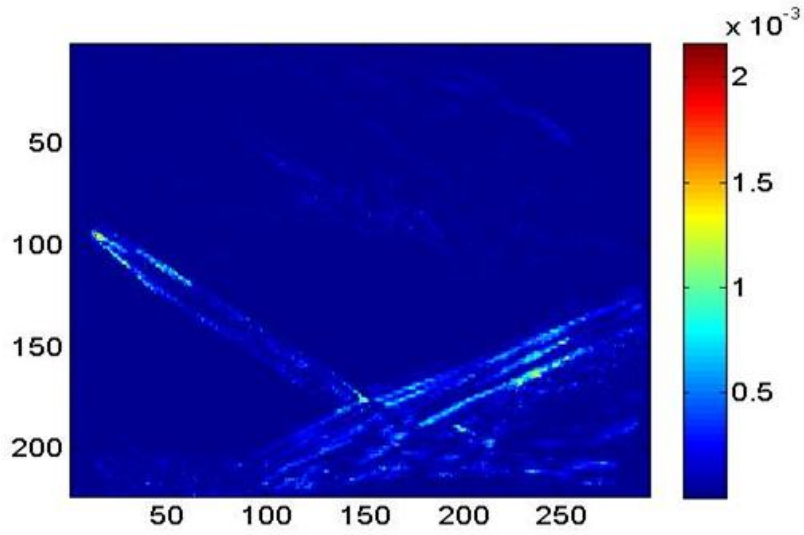


Figure 5.25 Power spectrum at 390.64 Hz

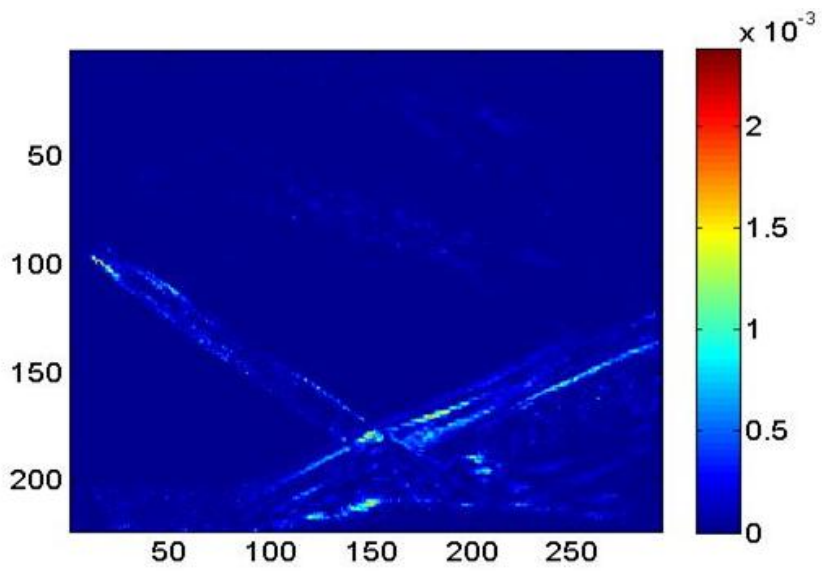


Figure 5.26 Power spectrum at 415.05 Hz

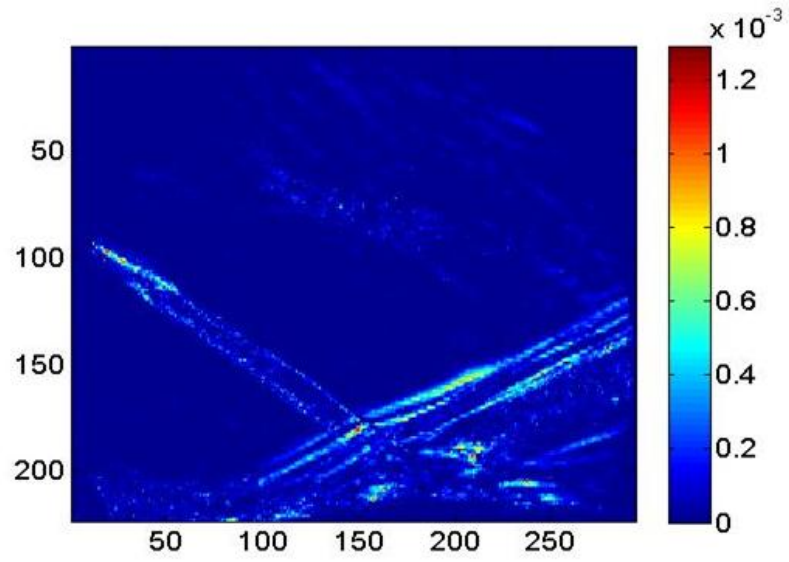


Figure 5.27 Power spectrum at 439.47 Hz

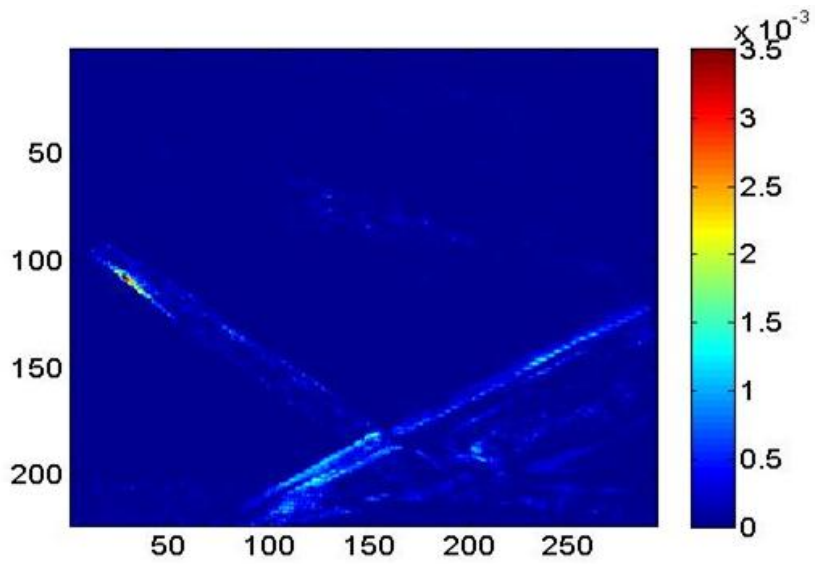


Figure 5.28 Power spectrum at 463.88 Hz

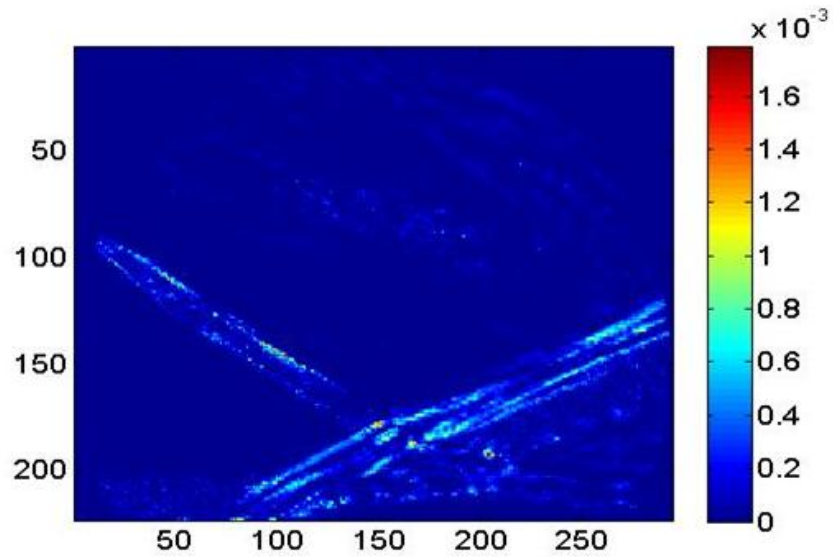


Figure 5.29 Power spectrum at 488.30 Hz

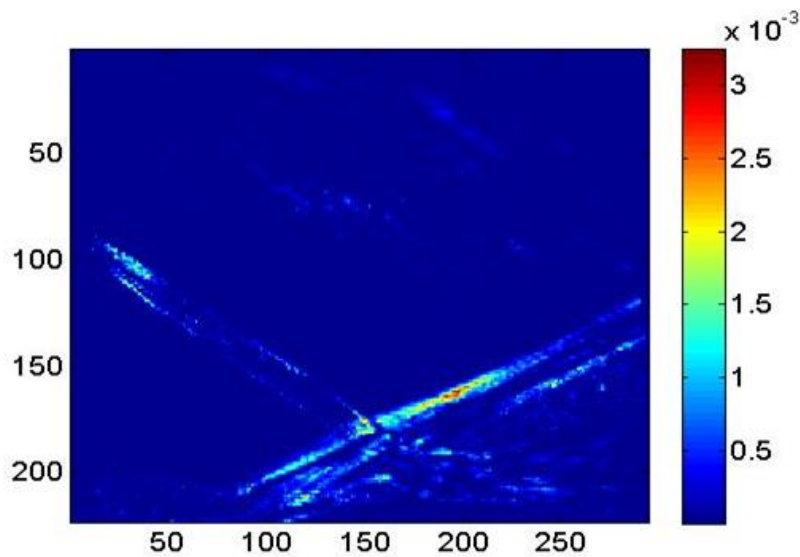


Figure 5.30 Power spectrum at frequency of 500 Hz

Figures 5.25 through 5.30 shows that for the frequencies in the range of 390.64Hz to 500Hz, most of the high power spectral density values are concentrated in the region of the reflected shock close to the point of interaction and in the region of the foot of reflected shock. In all of these cases, the relaxation zone has a considerable amount of variation of power spectra

values, which can be the reason for the unsteadiness of the flow downstream of the separation region. It could be stated that this variation of the power values at these frequencies are due to the fluctuations in the flow field, which on a whole causing the separation.

Within the 244.15Hz to 500Hz frequency range, the higher power spectrum values are located in the regions close to the separation region in the recirculation zone. It has been identified from Dussauge et al(2006) that the frequency at which maximum value of power spectrum occurs in the region of the recirculation zone close the wall can be treated as the dominant frequency. Similar study has been mentioned in the paper by Dussauge and Piponniau (2008) in their study of shock boundary layer interaction from an oblique shock.

Erengil and Dolling(1991) have identified a dimensionless shock frequency or Shock Strouhal number as $S_L = f_s L / U_e$ where f_s is the characteristic shock frequency, L is the length of interaction and U_e is the external velocity. In this expression, f_s correspond to the frequency where maximum power spectral values occur. In the current experiment the f_s is considered in the region close to the foot of the reflected shock and just above the separation bubble. The length of the interaction is obtained by calculating the distance between the mean point at the foot of the reflected shock and the extrapolation point onto the wall of the incident shock. The length of interaction calculation is explained in further paragraphs. U_e here as explained is the free stream velocity of the flow, which in our experiment was 601.18 m/s.

In the current scenario, the length of interaction has been calculated using MATLAB code written for this purpose. Canny edge detection algorithm has been used to find the edges in the entirety of each image of the color schlieren images. A similar approach was done by Estruch et al (2008) in measurement of shock wave unsteadiness using high speed schlieren system using digital image processing. The edges of the foot of the reflected shock which form a comb like

structure are identified. It has been noted that this comb like structure oscillates in a to and fro motion and hence does not have a fixed position of origin. The oscillations can be considered as to move around a mean point and the goal is to find that mean point to calculate the length of interaction. As the edges are detected for 1024 images, the pixel locations are obtained for the comb like structure. In this experiment we have found both mean and median point of the foot of the reflected shock. An extrapolated point on the wall has been obtained for the incident shock which is where the incident shock supposedly hits the wall. Then the length of the interaction has been calculated which gave us in pixels. This when multiplied with the actual pixel length of 0.259mm gave us the actual length of interaction. The length of interaction when calculated using the mean point was 36mm and when calculated using the median point was 32.9mm. The sample image with the edges can be seen in the Figure 5.31

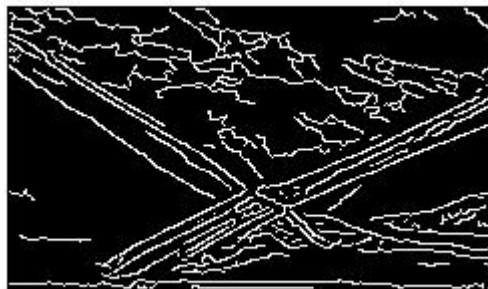


Figure 5.31 Edge detection on the color schlieren images

Hence based on the length of interaction, dominant frequency range and the free stream velocity, we had obtained Strouhal numbers both for lengths with respect to mean point of the foot of the reflected shock and median point of the foot of the reflected shock. The Strouhal number range was 0.0145 – 0.029 when length of interaction was with respect to mean point of the foot of the reflected shock. The Strouhal number range was 0.013 – 0.027 when the length of interaction was with respect to the median point of the foot of the reflected shock. This range of Strouhal

numbers, when compared to the other oblique shock experiments from the references is a close match, as most of them were in the range of 0.02 – 0.05.

5.3 Snapshot Proper Orthogonal Decomposition results

The data obtained in the form of displacements has also been used in the Snapshot Proper Orthogonal Decomposition, technique to calculate the flow structures that can be sorted with respect to their energy content. POD decomposes the flow fields into a series of POD modes with corresponding coefficients based on the orthogonal eigenfunctions. These eigenfunctions are used to extract the coherent structures from the flow fields. In this experiment the pictures are taken at a high speed rate which allows us to analyze them with respect to time. The temporal correlation matrices were built by using the pixel wise hue values throughout the set of images. Using the analysis procedure explained earlier for the Snapshot POD, the Eigen values and Eigen vectors for the time correlation tensor are calculated. The Eigen values correspond to the energy contained within that mode. The total amount of energy associated with the flow field can be calculated by summing all the Eigen values. As the Eigen value matrix is a diagonal matrix, the summation of the Eigen values is the trace of the Eigen value matrix. The variation of the energy with respect to each mode can be seen in the table and the figure in Appendix B.

In the current experiment it has been noted that the highest energy associated with the modes is with the last mode. This mode contributes a substantial portion of the total energy of the flow and hence plays a significant role in determining the flow dynamics than the mode that contains less energy (Kostas et al 2005). Hence the last Eigen mode has been studied for the dominant flow structure and unsteadiness in the boundary layer interaction. The energy associated with other modes decays fast that the energy associated with the other modes is

relatively very small (Berkooz et al 1993). The same has been identified in our experiments where in energy associated with the modes other than the highest energy mode is of very small magnitude. If other POD studies are considered for comparison about the energy association, Bernero & Fiedler (2000) have reported about 20 modes contains appreciable amount of energy (75% of total energy) in their study of jet in counter-flow, similarly Patte-Rouland et al (2001) have found that 60 modes were required to capture 75% of energy in their study of annular jet. In our experiment, we have found that to obtain 90% of the total energy 15 modes were required. Majority of the energy was concentrated in the last Eigen mode which was considered as the highest energy mode. The energy associated with the highest energy modes was found to be 19.8 units and the total percent of energy associated with this mode is 84.5 percent of the total energy. The second highest energy mode's energy was observed to be 0.46 units. Whereas rest of the modes have energy less than 0.2 units. And as we move further down from the highest energy mode the energy values as explained earlier decayed faster and were observed close to zero. Similar rapid decay of energy was also observed in other studies as mentioned earlier. The total amount of energy was calculated as by summing up energies of each mode as explained in the analysis section and thus it was observed to be 23.41units. The following discussion proceeds with the explanation of the flow field associated with energy modes. The flow field associated with the highest energy POD mode is shown in Figure 5.32

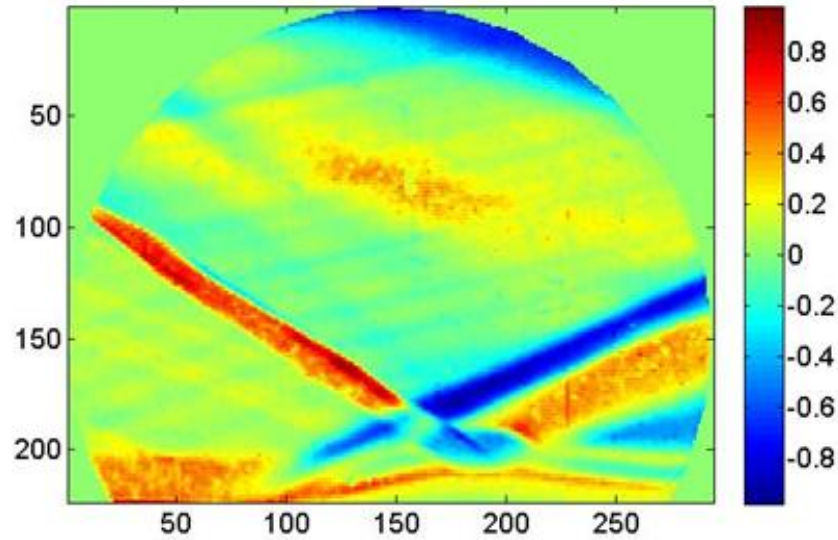


Figure 5.32 Average deflection length calculated using the highest energy mode

The Figure 5.32 which is the flow field associated with the highest energy mode resembles the ensemble averaged deflections. It is noted that in this mode we can observe the major flow phenomenon which is the impinging shock, the incoming turbulent boundary layer, foot of the reflected shock, the separation bubble region and the reflected shock, the expansion region below it and the compression waves downstream the separation bubble The Figure 5.33 displays the flow field associated with the combination of modes apart from the highest energy mode.

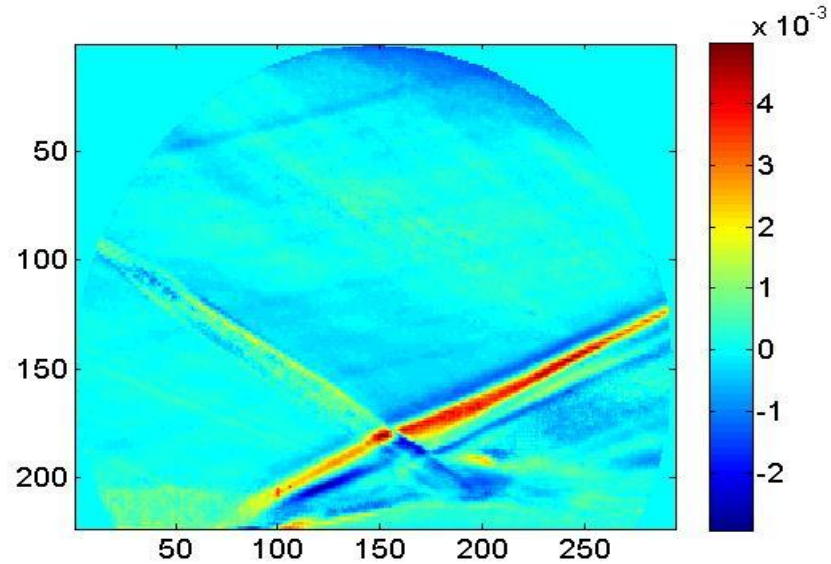


Figure 5.33 Average deflection length calculated using the other modes

The advantage of the POD is to obtain the flow structure associated with modes such that any variation in the flow field can be analyzed with respect that particular energy mode. From the figure 5.33 which corresponds to the flow field using the combination of the other modes, it can be seen that positive and negative deflections were more in the region of the incoming shock, reflected shock and just above the separation bubble and in the expansion region but with very less magnitude as compared to the flow field with highest energy mode. The flow fields with respect to the modes which are lower in energy than the highest energy mode are described as follows. The flow with respect to energy corresponding to the second highest energy mode is shown in the following Figure 5.34.

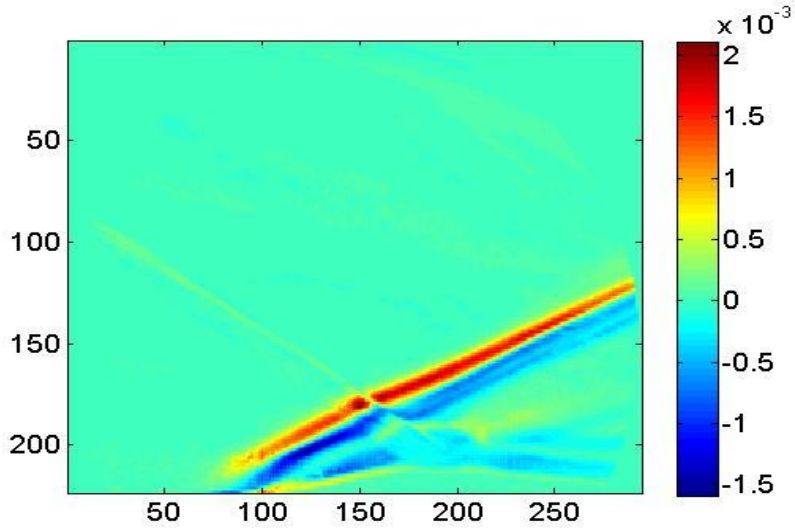


Figure 5.34 Average deflection length calculated using second highest mode

From Figure 5.34, it can be observed that the energy of the flow field which is associated with the second highest energy mode is more concentrated in the region of the reflected shock and at the foot of the reflected shock and portion of recirculation zone. It is clearly seen from the figure that the decay in energy is rapid which can be seen from the magnitudes of the deflections. The flow corresponding to the third highest energy mode can be seen in Figure 5.35.

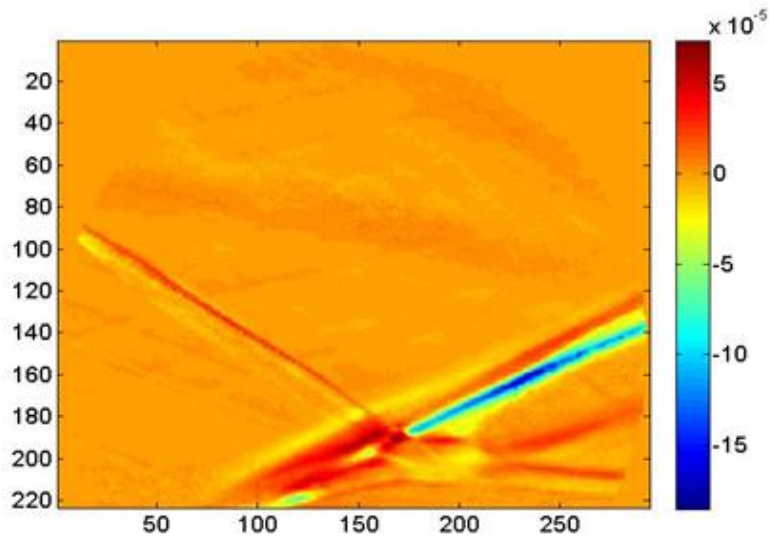


Figure 5.35 Average deflection length calculated using the third highest mode

In this case as from Figure 5.35, major deflections that can be seen are in the interaction region, close to the foot of the reflected shock. It can also be observed that there is considerable amount of deflection in the incident shock and also near the expansion region downstream the recirculation zone. The negative deflections can be seen in the region of the reflected shock which are also high, but of negative order.

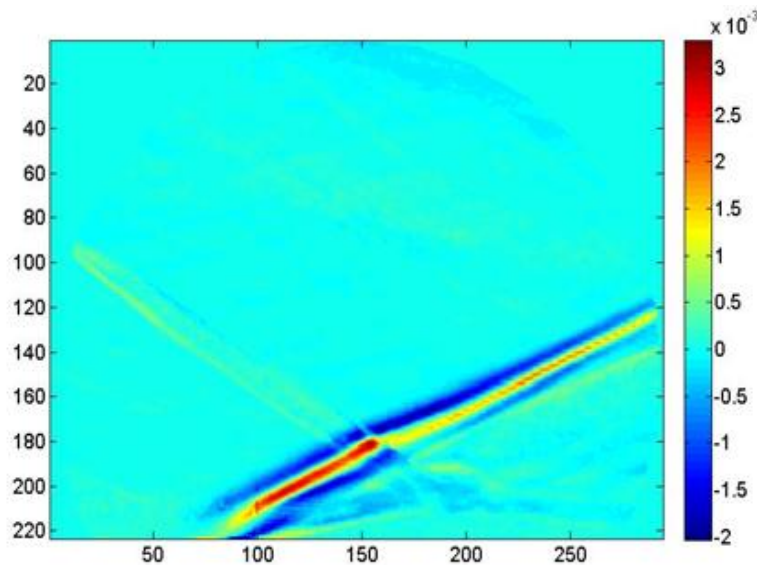


Figure 5.36 Average deflection length calculated using fourth highest mode

Figure 5.36 displays the flow field associated with the fourth highest energy mode. In this case, we can see that both positive and negative displacements are high in the foot of the reflected shock region. These deflections can be associated with the shock motion as they are dominant in this particular energy mode.

Figures 5.37 to 5.42 were used to study the flow fields which correspond to the weaker energy modes which also represent less energy zone regions.

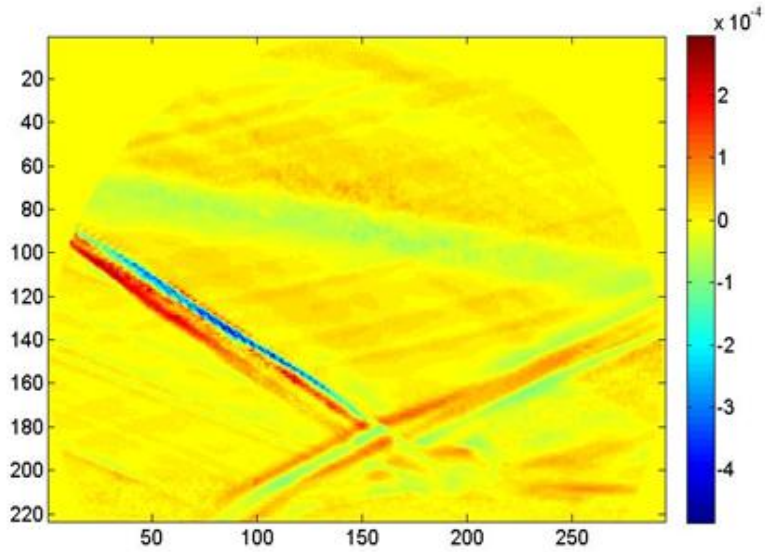


Figure 5.37 Average deflection length calculated using the fifth mode

From the above figure 5.37, it can be observed that the less energy zone is in the recirculation and the relaxation zone downstream the separation bubble. It is to be noted that at this node the deflections in the incident shock are higher and this flow structure is prominent in this mode.

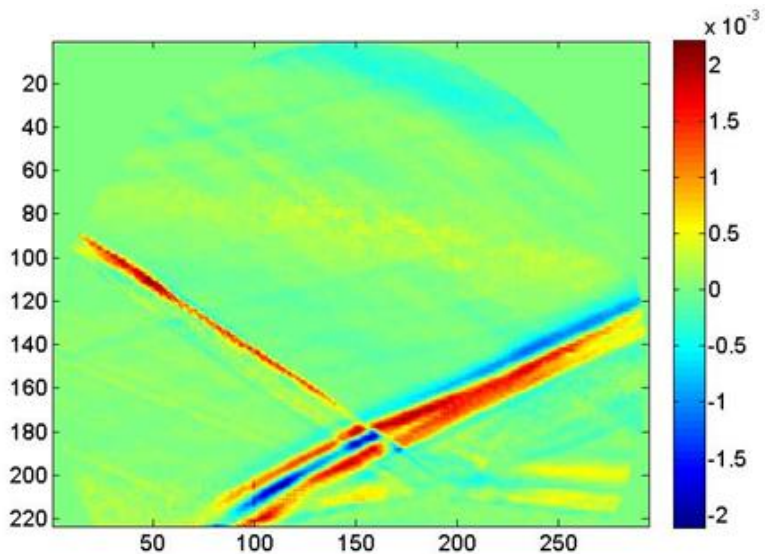


Figure 5.38 Average deflection length calculated using the sixth mode

It is also noted from figure 5.38 that lesser energy is concentrated in the recirculation and relaxation region and the higher deflections are observed in the reflected shock and the foot of the reflected shock.

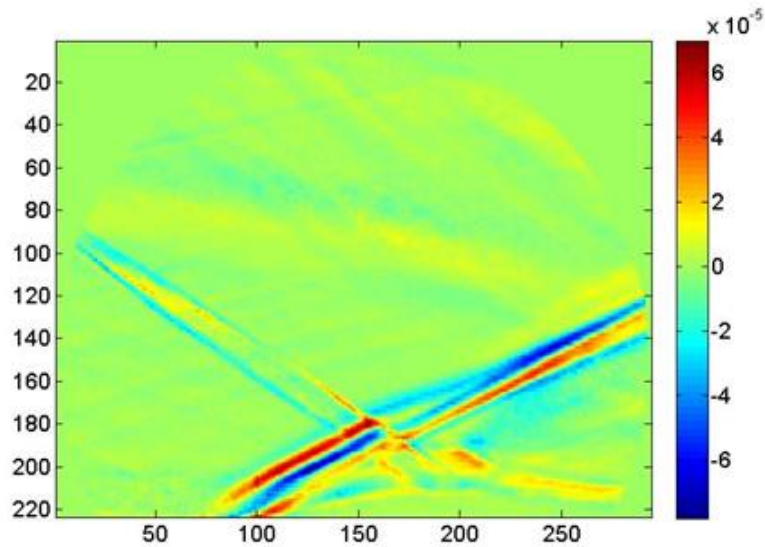


Figure 5.39 Average deflection length calculated using the seventh highest mode

From the figure 5.39 it is to be noted that the prominent flow structure associated here in this node is the combination of the incident and reflected shock.

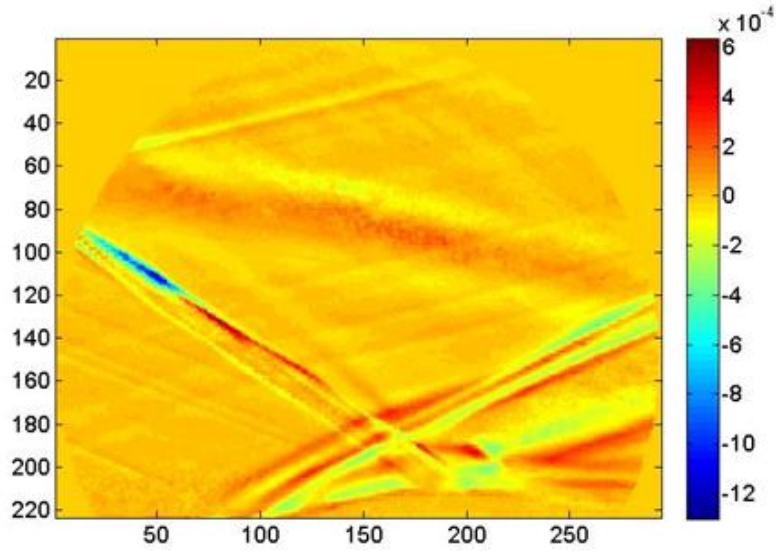


Figure 5.40 Average deflection length calculated using the eighth mode

It can be seen from the figure 5.40 that most of the deflections that are found in major portion of the flow field are the positive deflections. And these positive deflections were found to be spread in the region of the interaction and also in the compression waves of the relaxation region.

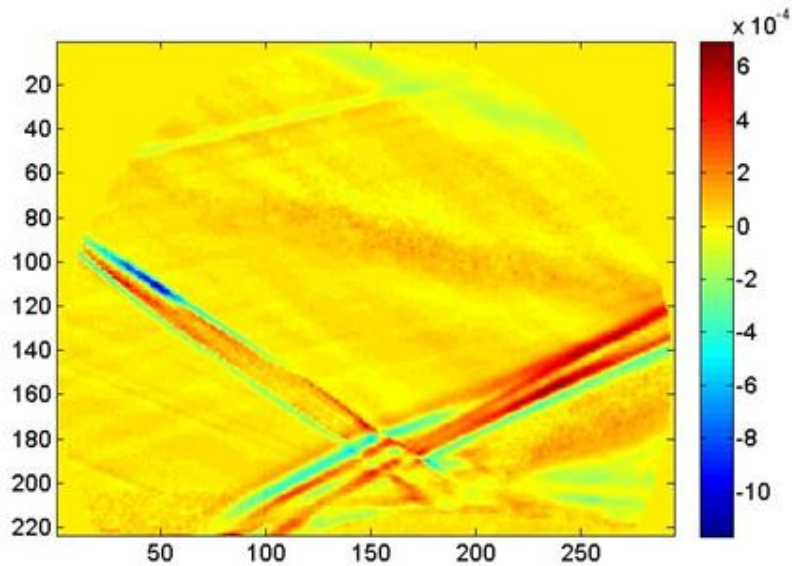


Figure 5.41 Average deflection length calculated using the ninth highest mode

It can be deduced from figure 5.41 that the positive deflections are higher in the reflected shock however there are negative deflections in the foot of the reflected shock and also near the expansion region. Higher negative deflections were found in the incident shock.

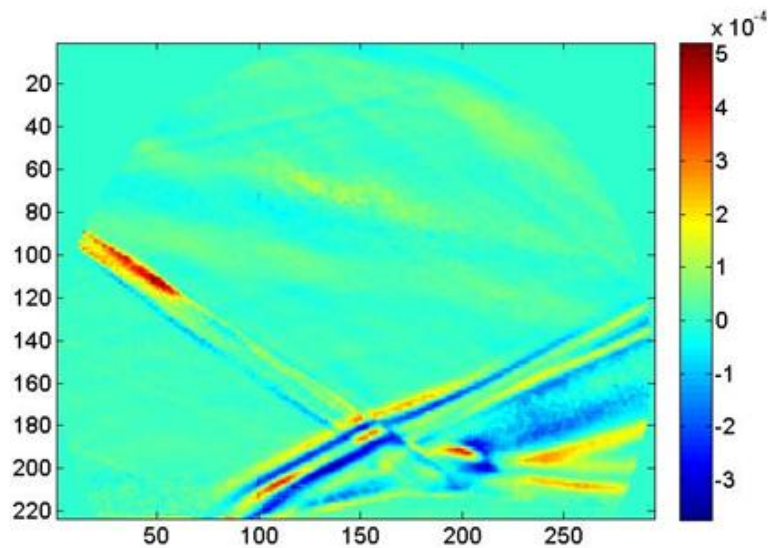


Figure 5.42 Average deflection length calculated using the tenth highest mode

From the above figure 5.42 which displays the deflections of the tenth highest energy mode the flow field prominent this mode is the recirculation region and as it can be seen that the major deflections that occur in this region are the negative deflections.

If we observe the displacements from the fourth highest through tenth highest energy modes, a shift in the displacements can be noticed in different regions. That is in the fourth and fifth highest energy mode the deflections were concentrated in the incident shock, reflected shock. In the sixth highest energy mode, the deflections are more in the reflected shock. Whereas in the seventh highest mode, the deflections are more in the region of the interaction and downstream of the recirculation zone, which is the relaxation zone. In eighth and ninth highest modes, more deflections concentrated in the expansion region and in the relaxation zone.

But the magnitude of the deflections are less compared to the other modes as the energy rapidly decreases as we move farther from the highest energy mode. The deflections in the tenth highest energy mode were observed to be further less compared to the other higher energy modes and the concentration of the deflections were more in the recirculation zone. Similarly it was noticed that as we move further down with the energy modes which are away from the highest energy mode, the magnitude of displacements also tend towards much lower values.

CHAPTER 6

CONCLUSION AND FUTURE WORK

Rainbow Schlieren Deflectometry in conjunction with image processing and Snapshot Proper Orthogonal Decomposition have been used effectively to study the flow structure of the shockwave boundary layer interaction of an oblique shock originating from a wedge of 12° inclination. The deflections calculated using the hue values of the images were observed to be large along the compression, expansion region and surrounding the separation bubble indicating large density gradients in these regions. The ensemble averaged deflection images were used to calculate average density gradients around which the hue displacements fluctuated. Local density gradients have been used to figure out the pixel wise density values of the color schlieren images by integration. The density contour thus obtained displayed the variations of density in the images based on the compression and expansion region and the recirculation region.

Based on the Fourier analysis, the flow structure was analyzed with respect to the frequencies. Peak frequency contour has given us the maximum value of the frequency that can occur at a particular pixel. Based on the individual frequencies, the power spectral values were obtained and the frequency range corresponding to the maximum power spectral values were obtained as the dominant frequency. The length of interaction has been studied with respect to the mean point and median point of foot of the reflected shock in the process of Strouhal number calculation. The Strouhal number obtained was in agreement with the number obtained from other experiments. Thus based on the Fourier transform analysis and the Strouhal number obtained in this study which is in accordance with the other studies also suggests that the unsteadiness may be attributed to the low frequencies present in the flow near the foot of the reflected shock.

The low frequency influence on the reflected shock motion has been identified by the frequency and the power spectral analysis. It may need further work for proving a relation in between shock motion and low frequencies that exist near the foot of the shock and in the recirculation region. Based on the fluctuations and the variation in distribution of the peak frequencies in the region downstream of the recirculation region, it has been identified that the flow is unsteady past the separation.

Snapshot POD has been used to analyze the dominant structure and corresponding structures with respect to the highest energy mode and with energy modes excluding the highest energy mode. The total energy associated with the modes has been identified and corresponding highest energy mode is obtained. Based on highest energy mode, the dominant flow structure has been found, which resembles the ensemble averaged deflections output. It has been identified that the dominant structure similar to the ensemble averaged deflections, but there are some differences in it as the highest energy mode does not contain total energy in it. The structures associated with the other modes subsequent to the highest energy mode have been analyzed. It has also been identified how the flow structure varies with respect to the other energy modes and how the flow structure varies with energy mode. It has been identified how the dominant regions in the flow varies with the corresponding change of the POD mode. Future progress can be made in using these techniques to develop better understanding and to develop methods to study the unsteady aspect of the flow structure of SWBLI.

REFERENCES

- Ferri A., "Experimental Results with airfoils tested in the High-speed Tunnel at Guidonia", Atti. Di Godonia, No. 17, 1939, Eng. Trans. 1940.
- Jean Delery, Jean-Paul Dussauge, "Some physical aspects of shock wave/boundary layer interaction" Shock Waves (2009), Volume: 19, Issue: 6, Pages: 453-468
- Jean M. Delery, "Shock wave/turbulent boundary layer interaction and its control" Progress in Aerospace Sciences, Volume: 22, Issue: 4, Pages: 209-280, 1985
- Dolling, D.S., 2001, "Fifty Years of Shock-Wave/Boundary-Layer Interaction Research: What Next?" AIAA Journal, Vol. 39, No. 8, August.
- Settles, G. S. and Dodson, L. J., 1994, "Supersonic and Hypersonic Shock/Boundary-Layer Interaction Database." AIAA Journal, Vol. 32, No. 7, July, pp. 1377-1383.
- Pirozzoli, S., and Grasso, F., "Direct numerical simulation of impinging shock wave/turbulent boundary layer interaction at $M=2.25$." Physics of Fluids, Vol. 18. 2006.
- Dussauge, J. P., Dupont, P., and Debieve, J. F., "Unsteadiness in shock wave boundary layer interactions with separation." Aerospace Science and Technology, Vol. 10, pp. 85-91. 2006.
- Piponniau, S, Dussauge, J. P, Debieve, J. F, Dupont, P, "A simple model for low-frequency unsteadiness in shock-induced separation", Journal of Fluid Mechanics, 25 June 2009 629: pp 87-108.
- Kleine H, Groenig H, "Color schlieren methods in shock wave research", Shock Waves, Vol. 1, p. 51-63, March 1991.
- Burt W. Albers and Ajay K. Agrawal, "Schlieren Analysis of an Oscillating Gas-Jet Diffusion Flame", Elsevier, Combustion and Flame, Volume 119, number 1, pp. 84-94, October 1999.
- Sugiyama, Hiromu; Minato, Ryojiro; Mizobata, Kazuhide; Tojo, Akira; Muto, Yohei, "Study on shock wave and turbulent boundary layer interactions in a square duct at Mach 2 and 4" Journal of Thermal Science, Volume 15, Issue 1, pp.37-42
- Dong Yang, Ran Huo, Longhua Hu, Xiaoyuan Xu, Fei Tang, Shi Zhu, Yaqiang Jiang, "The Application of Snapshot POD method in characterization and analysis of numerically simulated fire-induced flows", Proceedings of the ASME Heat Transfer Summer Conference, HT2009, July 19-23, 2009, San Francisco, California USA

- Hilberg D, Lazik W and Fiedler H.E, “The application of classical POD and snapshot POD in a turbulent shear layer with periodic structures”, *Applied Scientific Research*, Vol. 53, pp 283-290, 1994.
- Roi Gurka, Alexander Liberson, Gad Hetsroni, “POD of vorticity fields: A method for spatial characterization of coherent structures”, *International Journal of Heat and Fluid Flow*, Vol 27, pp. 416-423, 2006.
- Mandar V. Tabib, Jyeshtharaj B. Joshi, “Analysis of dominant flow structures and their flow dynamics in chemical process equipment using snapshot proper orthogonal decomposition technique ”, *Chemical Engineering Science*, Vol. 63, pp. 3695-3715, 2008.
- Dussauge J.P, Piponnier S.,”Shock/boundary-layer interaction: Possible sources of unsteadiness”, *Journal of Fluids and Structures* 24 (2008) 1166–1175
- Estruch D., Lawson N.J., MacManus D.G., Garry K.P, and Stollery J.L, “Measurement of shock wave unsteadiness using a high-speed schlieren system and digital image processing”, *Citation: Rev. Sci. Instrum.* 79, 126108 (2008)
- Erengil M.E, Dolling D.S, Unsteady wave structure near separation in a Mach 5 compression ramp interaction, *AIAA J.* 29 (5) (1991)
- Piponnier S., Collin E, Dupont P, Debieve J. F, “Simultaneous wall pressure – PIV measurements in a shock wave / turbulent boundary layer interaction”, *Seventh International Symposium on Turbulence and Shear Flow Phenomena*, 2011, July 28-31, Ottawa, Canada
- Kostas J., Soria J., Chong M. S., “A comparison between snapshot POD analysis of PIV velocity and vorticity data” *Experiments in Fluids* 38 (2005) 146–160
- Patte-Rouland B., Lalizel G., Moreau J and Rouland E., “Flow analysis of an annular jet by particle image velocimetry and proper orthogonal decomposition” *Measurement Science and Technology*. 2001, 1404 – 1412.
- Berkooz G., Holmes P., and Lumley J. L., “The Proper Orthogonal Decomposition in the Analysis of Turbulent Flows”, *Annual Review of Fluid Mechanics*, 1993
- Bernero S., Fiedler H.E., Application of particle image velocimetry and proper orthogonal decomposition to the study of a jet in a counterflow, *Experiments in Fluids*, 2000
- Dolling D.S., Brusniak L., Separation shock motion in fin, cylinder, and compression ramp-induced turbulent interactions, *AIAA Journal*, Vol. 27, 1989.
- Wu M. and Martin P., “Analysis of the shock motion in shockwave and turbulent boundary layer interaction using direct numerical simulation data”, *Journal of Fluid Mechanics*, 2008.

Humble R.A., Scarano F., Van Oudheusden B.W., “Unsteady aspects of an incident shockwave/turbulent boundary layer interaction” *Journal of fluid mechanics*, 2009.

Dupont P., Haddad C., Ardissonne J.P, Debieve J.F., “Space and time organisation of a shock wave/turbulent boundary layer interaction”, *Aerospace Science and Technology*, 2005.

APPENDIX

APPENDIX A

Table A.1 Free stream conditions

| Mach | Velocity, m/s | Temperature, K | Pressure, Psi |
|------|---------------|----------------|---------------|
| 3.0 | 601.1 | 100.7 | 1.65 |

Table A.2 Pressure regulator conditions

| Pressure, Psi | Temperature , K |
|---------------|-----------------|
| 65 | 288 |

APPENDIX B

Table B.1 Energy associated with POD modes

| POD mode | Energy associated | | | | | |
|----------|-------------------|--|--|--|--|--|
| 1 | 0.000493956 | | | | | |
| 2 | 0.000497445 | | | | | |
| 3 | 0.000499233 | | | | | |
| 4 | 0.000501525 | | | | | |
| 5 | 0.0005034 | | | | | |
| 6 | 0.000505483 | | | | | |
| 7 | 0.000506438 | | | | | |
| 8 | 0.000506893 | | | | | |
| 9 | 0.000509146 | | | | | |

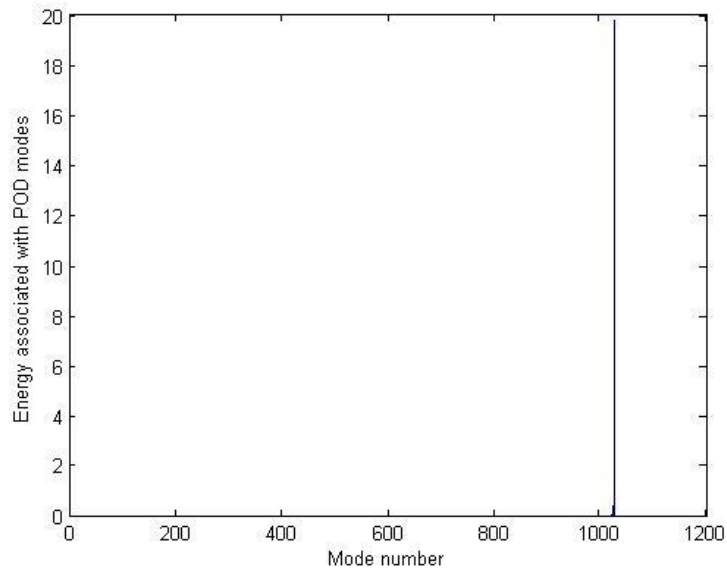


Figure B.1 Energy associated with POD modes

APPENDIX C

MATLAB Code for data reduction:

Data reduction has been performed using MATLAB codes. The source code of five programs used in the processing of the color schlieren images are documented in this section:

C.1 Cromptestdata.m, which reads the file names of color schlieren images using an input file which contains information such as how a file name starts, how many files are present in the directory, which file to read and the increment details. The program then crops the image to the desired dimensions so as to facilitate analysis in the desired region of interest. The input file can be any text editor file. Notepad has been used in the current work.

C.2 Calib.m, which also requires an input file which contains information such as how a file name starts, how many files are present in the directory, which file to read and the increment details.. The code then identifies the hue associated with each image and compares with the background image and gives the hue, displacement and standard deviation values corresponding to the background hue value.

C.3 Basecode.m, which reads in the test images from the given folder and calculates the deflection of hue values with respect to the background hue and from then on calculates the ensemble averaged deflections, density gradients, density and their corresponding RMS values. Using the same information, it further performs the fast fourier transform on the deflections and also calculates the power associated with the frequency. Further snapshot proper orthogonal decomposition is performed on the deflections to find out the dominant flow field associated with the highest energy mode and flow field associated with other energy modes.

C.4 Lengthofinteraction.m, which reads the color schlieren test images and detects the edges in them. Based on the edges detected the program finds out the distance between the points where the reflected shock foot is generated and finds the median value and mean value of those points and the extrapolated point that supposedly touches the wall.

C.1 Croptestdata.m

```
function [] = croptestdata()
clear all
clc
fid = fopen('input.dat','rt');
[name] = fscanf(fid,'%3c',[1]);
fprintf (strcat(name,'\n'))
[a] = fscanf(fid,'%g',[1,2]);
[num] = a(1);
[dd] = a(2);
fprintf (strcat('number of files :',num2str(num),' , incremental distance
:',num2str(dd),'\n'))
[b] = fscanf(fid,'%d',[1,2]);
[nums] = b(1);
[in] = b(2);
fprintf(strcat('starting number :',int2str(nums),' , increment
:',int2str(in),'\n'))

for ifile = nums-1:num
    if ifile < 10
        file = strcat(name,'000',int2str(ifile),'.tif');

    elseif (ifile >= 10)&(ifile < 100)
        file = strcat(name,'00',int2str(ifile),'.tif');
    elseif (ifile >= 100)&(ifile < 1000)
        file = strcat(name,'0',int2str(ifile),'.tif');

    else
        file = strcat(name,int2str(ifile),'.tif');

    end
    [grayImage] = imread(file,'tif');

% Read in image
grayImage=rgb2hsv(grayImage);
grayImage=grayImage(:, :, 1);
imshow(grayImage);
hFH=imellipse(gca,[94.4776951672863 56.5297397769515 293.353159851301
299.063197026022]);

% Create a binary image ("mask") from the region of interest in the object.
binaryImage = hFH.createMask();
```

```

% Get coordinates of the boundary
structBoundaries = bwboundaries(binaryImage);
xy=structBoundaries{1}; % Get n by 2 array of x,y coordinates.
x = xy(:, 2); % Columns.
y = xy(:, 1); % Rows.

% Burn line into the given image by setting it to 255 wherever the mask is
true.
burnedImage = grayImage;
burnedImage(binaryImage) = 255;
blackMaskedImage = grayImage;
blackMaskedImage(~binaryImage) = 0;

% Repeat above procedure but blacken the inside region.
insideMasked = grayImage;
insideMasked(binaryImage) = 0;

% crop the image.
topLine = min(x);
bottomLine = max(x);
leftColumn = min(y);
rightColumn = max(y);
width = bottomLine - topLine + 1;
height = rightColumn - leftColumn + 1;
croppedImage = imcrop(blackMaskedImage, [topLine, leftColumn, width,height]);

% write the image in the same folder

croppedImage=imcrop(croppedImage,[0.5 0.5 294 222]);

    imwrite(croppedImage,file,'tif');

end

fclose(fid);

```

C.2 Calib.m

```
function [] = calib()
clear all
clc
fid = fopen('input.dat','rt');
[name] = fscanf(fid,'%3c',[1]);
fprintf (strcat(name,'\n'))
[a] = fscanf(fid,'%g',[1,2]);
[num] = a(1);
[dd] = a(2);
fprintf (strcat('number of files :',num2str(num),' , incremental distance
:',num2str(dd),' \n'))
[b] = fscanf(fid,'%d',[1,2]);
[nums] = b(1);
[in] = b(2);
fprintf(strcat('starting number :',int2str(nums),' , increment
:',int2str(in),' \n'))
[c] = fscanf(fid,'%d',[1,2]);
[wo] = c(1);
[ho] = c(2);
fprintf(strcat('origin pixel coordindates (Upper Left)','wo = ',int2str(wo),'
ho = ',int2str(ho),' \n'))
[d] = fscanf(fid,'%d',[1,2]);
[ws] = d(1);
[hs] = d(2);
fprintf(strcat('image pixel size (Lower Right)','ws = ',int2str(ws),' hs =
',int2str(hs),' \n'))
fclose(fid);
if in < 10
    file = strcat(int2str(name),'00',int2str(in),' .txt');
elseif (ifile >= 10)&(ifile < 100)
    file = strcat(int2str(name),'0',int2str(in),' .txt');
else
    file = strcat(int2str(name),int2str(ifile),' .txt');
end
fid = fopen(file,'wt');
for ifile = nums:num
    if ifile < 10
        file = strcat(name,'00',int2str(ifile),' .tif');
    elseif (ifile >= 10)&(ifile < 100)
        file = strcat(name,'0',int2str(ifile),' .tif');
    else
        file = strcat(name,int2str(ifile),' .tif');
    end
    [tiff] = imread(file,'tif');
    [x] = rgb2hsv(tiff);
    hue = x(:, :, 1).*360; clear x
    hue=imcrop(hue, ([115.5 121.5 250 160]));
    ahue = mean(hue(:));
    sd = std(hue(:), 1);
    dis = (ifile-1)*dd;
    fprintf(fid,'%g %g %g', dis, ahue, sd);
    fprintf(fid,'\n');
    hu(ifile-nums+1) = ahue;
    distance(ifile-nums+1) = dis;
```

```
    std_deviation(ifile-nums+1) = sd;
end
fclose(fid);
X = distance; H = hu; Stderr = std_deviation;
save('filter_calibration.mat', 'X', 'H', 'Stderr');
errorbar(distance, hu, std_deviation)
title('Filter Calibration Curve');
hold on
plot(distance, hu, '-r');
h1 = xlabel('Transverse displacement');
h2 = ylabel('Average Hue of image');
hold off
clear all
```

C.3 Basecode.m

```
clc
clear all
double all
format short
close all

numberoffiles=1024

% USING CALIBRATION CURVE TO CONVERT HUE TO DISPLACEMENT
% SUBTRACTING THE BACKGROUND HUE

calibrationim = imread('background.tif');
calibrationim=rgb2hsv(calibrationim);
backgroundhue=mean(mean(imcrop(calibrationim(:,:,1).*360,[117.5 129.5 247
147])));
load('C:\Users\narendra\Desktop\croppcirclebase\200micron-3mmfilter-
calibration\filter_calibration.mat','X','H');

range=63-11;
for i=1:range
    hue(i)=H(i+12);
    distance(i)=X(i+12);
end

zeroshift=interp1(hue,distance,backgroundhue,'linear','extrap')
distance=distance-zeroshift;
fclose(fid3)

% %ENSEMBLE AVERAGING TECHNIQUE
%TO CALCULATE THE MEAN AND THE FLUCTUATING deflection length and the density
%gradient fields
ind=zeros(223,294,numberoffiles);
imdeflect=zeros(223,294);
s=zeros(223,294);
ss=zeros(223,294);
fid2 = fopen('fnames.txt')
for ic=1:numberoffiles
    ic
    fname=fgetl(fid2);
    h=imread(fname);
    h=im2double(h);
    hh=h.*360;
    imdeflect=interp1(hue,distance,hh,'linear','extrap');
    imdeflect(imdeflect<=-3.0330)=0;
    dengrad=imdeflect/1000/(3*2.54/100*0.00023/1*750/1000);
    s=s+imdeflect;
    ss=ss+dengrad;
    ind(:,:,ic)=imdeflect(:,:,);
    ind2(:,:,ic)=hh(:,:,);
end

distmean=s/numberoffiles;
avedengrad=ss/numberoffiles;
```

```

fclose(fid2)

distflucsq=0;
dengradfluc=0;
indf=zeros(223,294,numberoffiles);
fid2 = fopen('fnames.txt');
for ic=1:numberoffiles
    ic
    fname=fgetl(fid2);
    h=imread(fname);
    h=im2double(h);
    hh=h(:, :, 1).*360;
    imdeflect=interp1(hue,distance,hh,'linear','extrap');
    imdeflect(imdeflect<=-3.0330)=0;
    dengrad=imdeflect/1000/(3*2.54/100*0.00023/1*750/1000);
    distflucsq = distflucsq + times((imdeflect-distmean),(imdeflect-distmean));
    dengradfluc=dengradfluc+times((dengrad-avedengrad),(dengrad-avedengrad));
    indf(:, :, ic)=imdeflect-distmean;
end
distfluc=distflucsq.^0.5/numberoffiles;
dengradfluc=dengradfluc.^0.5/numberoffiles;
fclose(fid2)

% CALCULATION OF THE DENSITY FIELD USING THE AVERAGE DENSITY GRADIENT VALUES
avedengrad=flipud(avedengrad);
figure(10);contourf(avedengrad)
pixlength=0.0102*25.4/1000;%in meters 1 pixel sees this length.
dens=zeros(223,294);
    densitydatum=1;
    datumrow=170;

for j=1:294
    dens(datumrow,j)=densitydatum;
    for i=datumrow:-1:2
        dens(i-1,j)=dens(i,j)-avedengrad(i,j)*(pixlength);
    end
    for i=datumrow:223
        dens(i+1,j)=dens(i,j)+avedengrad(i,j)*(pixlength);
    end
end

% % FFT ANALYSIS TO FIND THE MAX FREQUENCY VALUE AT EVERY PIXEL LOCATION
% using fluctuating deflection length values
%
Fs = 1000; % Sampling frequency
T = 1/Fs; % Sample time
L = numberoffiles; % Length of signal
NFFT = 2^nextpow2(L); % Next power of 2 from length of y
kcount=NFFT/2+1;
Py=zeros(223,294,kcount);
Yd=zeros(223,294,kcount);

for i=1:223
    i
    for j=1:294

```

```

        Y = fft(indf(i,j,:),NFFT)/L;
        for k=1:NFFT/2+1
            Py(i,j,k)=2*abs(Y(k));
        end
    end
end

maxPy=zeros(223,294);
I=zeros(223,294);

f = Fs/2*linspace(0,1,NFFT/2+1);
delf=(f(2)-f(1))
CX=Py(:, :, 2:kcount);
CZ=Py(:, :, 2:kcount).^2;
[C,I] = max(CX, [], 3);
I=I*delf;

% %Defining the Nt by Nt velocity correlation matrix givrn by their equation
phi=zeros(223,294,numberoffiles);
ind2=zeros(223,294,numberoffiles);
ind3=zeros(223,294,numberoffiles);
R=zeros(numberoffiles,numberoffiles);

for kk=1:numberoffiles
for ll=1:numberoffiles

        R(kk,ll)=sum(sum((ind(:, :, kk)).*(ind(:, :, ll))));

end
end
R=R/(384*512);
[V,D] = eig(R);
for nind=1:numberoffiles
    nind
for ic=1:numberoffiles
    phi(:, :, nind)=phi(:, :, nind)+V(ic,nind)*(ind(:, :, ic));    %forward transfer
to define the data in new coordinate systems
end
end

for ic=1:numberoffiles        %back tranfer using the dominant eigenmode
    ic
for nind=numberoffiles:numberoffiles
    ind2(:, :, ic)=ind2(:, :, ic)+V(ic,nind)*(phi(:, :, nind));
end
end
for ic=1:numberoffiles        %backward transformation using all the other
eigenmodes
    ic
for nind=1:numberoffiles-1
    ind3(:, :, ic)=ind3(:, :, ic)+V(ic,nind)*(phi(:, :, nind));
end
end

sss=0;

```

```

ssss=0;
for ic=1:numberoffiles           %finding the averaged image using the
dominant eigenmode and the other eigenmodes
sss=sss+ind2(:, :, ic);
ssss=ssss+ind3(:, :, ic);
end
sss=sss/numberoffiles;
ssss=ssss/numberoffiles;

save basecoderesults1024.mat

%PLOTTING THE FIGURES

figure(1);plot(distance,hue,'LineWidth',2)
set(gca,'FontSize',14)
xlabel('distance (mm)')
ylabel('hue')

figure(2);imagesc(distmean)
set(gca,'FontSize',14)
title('average deflection length (mm)', 'FontWeight', 'bold')
colorbar('eastOutside')
%

figure(3);imagesc(flipud(avedengrad))
title('average density gradient', 'FontWeight', 'bold')
colorbar ('EastOutside')

figure(4);imagesc(flipud(dens))
set(gca,'FontSize',14)
title('average density', 'FontWeight', 'bold')
colorbar ('EastOutside')

figure(5);imagesc((distfluc))
set(gca,'FontSize',14)
title('RMS fluctuating deflection length (mm)', 'FontWeight', 'bold')
colorbar ('EastOutside')

figure(6);imagesc((dengradfluc))
set(gca,'FontSize',14)
title('RMS fluctuating density gradient', 'FontWeight', 'bold')
colorbar ('EastOutside')

figure(7); imagesc((I))
set(gca,'FontSize',14)
title('max frequency (Hz)', 'FontWeight', 'bold')
colorbar ('EastOutside')

figure(7);mesh((I))
set(gca,'FontSize',14)
title('max frequency (Hz)', 'FontWeight', 'bold')
colorbar ('EastOutside')

```

```

k=325
for i=1:223
    for j=1:294
        P(i,j)=CZ(i,j,k);
    end
end
figure(325); imagesc((P))
set(gca,'FontSize',14)
title('power spectrum at 325Hz', 'FontWeight','bold')
colorbar ('EastOutside')

TE=trace(D)
figure(9),bar(1:ic,diag(D));
title('Energy');
xlabel('Mode number');
ylabel('Energy associated with POD modes');

figure(12); imagesc((sss))
set(gca,'FontSize',14)
title('average deflection length calculated using the most energetic mode',
'FontWeight','bold')
colorbar ('EastOutside')

figure(13); imagesc((ssss))
set(gca,'FontSize',14)
title('average deflection length calculated using the other modes',
'FontWeight','bold')
colorbar ('EastOutside')

```

C.4 Lengthofinteraction.m

```
clc
clear all
clc
numberoffiles=1024;

fid2 = fopen('fnames.txt')

for ic=1:numberoffiles
    ic
    fname=fgetl(fid2);
    x=imread(fname);
    x=rgb2hsv(x);
    x=x(:,:,1);
    xc=imcrop(x,[126.5 141.5 243 141]);

    c=edge(xc,'canny',[],1);

    for i=136:136
        for j=1:80
            if c(i,j,1)==1
                f(ic)= j;
                break
            end
        end
    end

end

end
f=f;
FM=median(f); %median point of reflected shock foot
QM=185-FM; %median length of interaction in pixels
q=185-f; %here 185 is the extrapolation point on the wall

b=0;
for n=1:numberoffiles
    n
    b=b+q(n);

end
figure(2),imshow(c)
avg=b/numberoffiles;
g=0.0102*25.4/1000; %pixel length
disp('average length of interaction in m')
avglength=avg*g % average length of interaction
disp('average length of interaction L in cm')
avglengthmm=avg*g*100
disp('length of interaction from median pt to extrapolated pt')
QM*g*100
```